

Universality of T -linear and B -linear Planckian scattering rate in high- T_c cuprate superconductors

K. Remund,^{1,2} K. V. Nguyen,² P.-H. Chou,^{1,2} P. Giraldo-Gallo,³ J. A. Galvis,⁴ G. S. Boebinger,^{5,6} and C.-H. Chung^{1,2,7}

¹Physics Division, National Center for Theoretical Sciences, Taipei 10617, Taiwan

²Department of Electrophysics, National Yang Ming Chiao Tung University, Hsinchu 30010, Taiwan

³Department of Physics, Universidad de Los Andes, Bogotá 111711, Colombia

⁴School of Sciences and Engineering, Universidad del Rosario, Bogotá, 111711, Colombia

⁵National High Magnetic Field Laboratory, Florida State University, Tallahassee, FL 32310, USA

⁶Department of Physics, Florida State University, Tallahassee, FL 32310, USA

⁷Center for Theoretical and Computational Physics (CTCP),

National Yang Ming Chiao Tung University, Hsinchu 30010, Taiwan

(Dated: February 12, 2026)

One of the long-standing puzzles in strongly correlated materials is the microscopic origin of the quantum critical Planckian strange metal phase with universal linear-in-temperature scattering rate from which unconventional superconductivity directly emerges by lowering temperatures. Recently, the linear-in-temperature and linear-in-field resistivity have been simultaneously observed in high- T_c cuprate superconductors, manifested by the universal field-to-temperature (B/T) scaling in magneto-resistivity. To date, there has been a lack of coherent and unified understanding of these co-existing linear behaviors and their possible link to quantum criticality. In this work, we establish the universality in T -linear and B -linear Planckian behaviors in underdoped LSCO near optimal doping. Experimentally, we observe the B -linear Planckian scattering rate and its relation to its T -linear counterpart. Theoretically, we propose a spin-based common microscopic mechanism based on Kondo-like charge fluctuations near local quantum criticality of heavy-fermion formulated t - J model subject to a Zeeman term. Similar to frequency-to-temperature (ω/T)-scaling near quantum criticality, we find the magnetic field here effectively introduces a Zeeman energy, reminiscent of an external energy ($\hbar\omega$) in the quantum critical regime, leading to B/T -scaling. Our analytically predicted universal B/T -scaling in isotropic scattering rate and the relation between the T -linear and B -linear Planckian coefficients, unifies these two phenomena over an extended doping range, pointing toward a unified quantum-critical origin of Planckian transport in cuprates.

I. INTRODUCTION

A major mystery in condensed matter systems is the microscopic origin of the strange metal with perfect linear-in-temperature resistivity extending to highest temperature without saturation, from which unconventional superconductivity directly emerges by lowering temperatures. In ordinary metals, however, electrical resistivity due to scattering among long-lived quasi-particles is bounded by the Mott-Ioffe-Regel (MIR) limit, where the mean-free path l cannot be shorter than the Fermi wavelength λ_F , $l \geq \lambda_F$. The T -linear resistivity in cuprates, which exceeds the MIR limit, is often referred to “Planckian dissipation”. This suggests a universal Planckian scattering rate in which transport relaxation rate $1/\tau$ is limited only by the thermal energy $k_B T$ (k_B is Boltzmann constant) divided by the universal constant \hbar ($\hbar = h/2\pi$ with h being Planck’s constant): $1/\tau = \alpha_T k_B T/\hbar$ with $\alpha_T \sim 1$ being a coupling-independent universal constant Planckian coefficient, instead of limited by the quasi-particle interaction strength. Experiments on overdoped cuprates have shown that this Planckian coefficient remains constant across different samples [1–7] and doping levels [8], indicating a universal state of matter. Meanwhile, frequency-to-temperature ($\hbar\omega/k_B T$) scaling from optical conductivity measurement [3] suggest that it is a quantum critical state.

To reveal the Planckian normal state of high- T_c cuprates and its link to putative quantum criticality inside the superconducting dome, magneto-transport measurements have been performed on various cuprates in high magnetic field to sup-

press superconductivity. The mysterious universal quantum-critical-like field-to-temperature (B/T) scaling in magneto-resistance in strange metal state has been observed in various cuprates over an extended doping range [10, 11], indicating this is a quantum critical “phase”. Interestingly, both linear-in-temperature and linear-in-field resistivity have been simultaneously observed therein, manifested more clearly by $k_B T \gg \mu_B B$ and $\mu_B B \gg k_B T$ limits of universal B/T -scaling in magneto-resistivity, respectively, suggesting a strong correlation between these two strange metal behaviors [11]. This suggests that both phenomena may share a common microscopic origin. To date, there has not been a unified and coherent understanding of these linear behaviors that co-exist in the regime of high fields ($B > 60$ T) and low temperatures ($T < 50$ K) (gray shaded areas in Fig. 1(a) and (b)). This puts challenges on our understanding of the magneto-transport in metals.

Magneto-resistance in ordinary metals originates from the cyclotron motion of electrons around the Fermi surface, determined by the product of cyclotron frequency, $\omega_c = eB/m^*$ (where m^* is the quasiparticle mass), and the quasiparticle relaxation time τ_B [12, 13]; consequently, the Kohler’s rule with quadratic-field magneto-resistivity $\rho(B)$ is expected: $\Delta\rho(B)/\rho(0, T) = f(B/\rho(0, T)) \propto (B/T)^2$ with $\Delta\rho(B) = \rho(B) - \rho(B = 0)$ [11]. The B/T -linear scaling in magneto-resistivity at high fields observed in cuprates clearly violates the Kohler’s rule, indicating that the field-dependent transport relaxation rate is set directly by the magnetic field through $1/\tau_B(B) = \alpha_B \mu_B B/\hbar$. Whether there exists a universal B -linear Planckian scattering rate $1/\tau_B(B) = \alpha_B \mu_B B/\hbar$ with

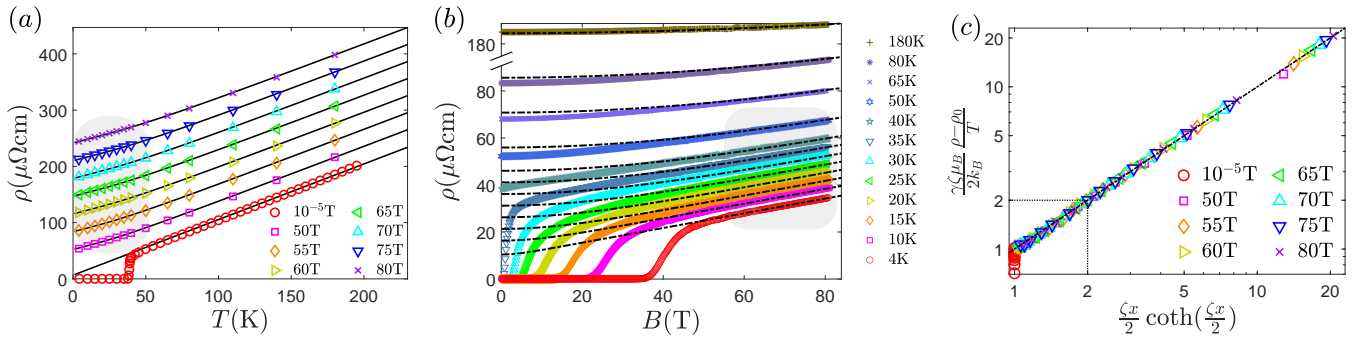


Figure 1. Magneto-resistivity data for LSCO at doping $p = 0.19$, in which T -linear and B -linear coexist over the range of temperatures ($T < 50\text{K}$) and magnetic fields ($B > 60\text{T}$) indicated by the shaded regions. (a) Magneto-resistivity versus temperature at different magnetic fields. Colored symbols represent experimental data and black solid lines correspond to the theoretical prediction given in Eq. (1), with $c_0 = 7.2\mu\Omega\text{cm}$, $c_1 = 0.654\mu\Omega\text{cmK}^{-1}$, $\gamma = 3.2(\mu\Omega\text{cm})^{-1}\text{T}$, $\zeta = 3.06$. For visibility purposes, the data points and curves have been shifted by $30\mu\Omega\text{cm}$ in the y-axis successively for each value of magnetic field. (b) Magneto-resistivity data versus magnetic field at different temperatures. Colored symbols represent experimental data and black dotted lines correspond to the theoretical prediction given in Eq. (1) with same fitting parameters values as in (a). (c) Scaling of the field dependent part of the magneto-resistivity at different magnetic field values in function of $\xi_x/2 \coth(\xi_x/2)$, with $x = \mu_B B/(k_B T)$. This is obtained by subtracting to the total magneto-resistivity the constant and temperature-only dependent ($\rho_0(T)$) and dividing it by temperature using the same parameters as in (a). Data is the same as in ref. [9] for LSCO.

$\alpha_B \sim 1$ in the same strange metal state of cuprates, similar to that in the corresponding T -linear counterpart is therefore an issue of great fundamental significance. If it does exist, whether a universality between these two Planckian metal behaviours and a possible common origin is an outstanding open problem.

Previous attempts to address this problem based on an orbitally driven origin include an approach based on Boltzmann transport of conventional electrons in the presence of an anisotropic Fermi surface [14], and the Sachdev-Ye-Kitaev-like models with extreme external disorder [15, 16]. However, it is still an open problem whether the former (semi-classical) approach—significantly relying on specific parametrization—is able to capture the generic and robust feature of the data: an extended regime of B -linear magneto-resistivity with universal quantum critical B/T -scaling [10, 11]. We note that recent experiments have demonstrated that the strange-metal behavior is independent of external disorder [17], which might pose challenges to approaches based upon SYK-like models.

In this work, we establish an unprecedented match between the experimental B -linear Planckian scattering rate and its relation to the T -linear counterpart near optimal doping of underdoped LSCO. We propose a spin-based common microscopic mechanism for this observation based on Kondo-like charge fluctuations near local quantum criticality via the recently developed heavy-fermion approach to the t - J model [18]. Within our approach, we assume the field-dependent scattering rate τ_B arises from the Zeeman splitting of fermions coupled to the isotropic component of the Fermi surface, a distinctly different approach than previous attempts based on electron orbital motion [14–16]. We find the isotropic electron scattering rate of our model near criticality simultaneously leads to both T -linear and B -linear resistivity. The Zeeman energy here plays a similar role as an external en-

ergy $\hbar\omega$ near criticality, giving rise to universal quantum critical B/T -scaling in transport, similar to ω/T -scaling observed in AC transport at zero field. Our analytically predicted universal B/T -scaling in scattering rate excellently unifies the T -linear and B -linear Planckian behaviors over an extended doping range, pointing toward a unified quantum-critical origin of Planckian transport in cuprates.

II. THEORETICAL MODEL: A UNIFYING FRAMEWORK FOR T -LINEAR AND B -LINEAR PLANCKIAN BEHAVIORS

The T -linear and B -linear resistivity have been simultaneously observed and systematically studied in the strange metal phase of LSCO over an extended doping range [9]. Inspired by this observation, we first look for signatures of quantum critical B/T -scaling by analyzing magneto-resistivity data in Ref. [9] at finite field and temperatures. We find magneto-resistivity can be decomposed into the following form (see Section III, Appendix B, and Ref.[18]):

$$\rho(B, T) = \rho_0(T) + \frac{k_B T}{\mu_B} \Phi\left(\frac{\mu_B B}{k_B T}\right),$$

$$\Phi(x) = \frac{x}{\gamma} \coth \frac{\xi_x}{2}, \quad (1)$$

with $x = \mu_B B/k_B T$, and $\rho_0(T)$ depends only on temperature but not fields and it shows T -linear behavior: $\rho_0(T) = c_0 + c_1 T$, and $\Phi(B/T)$ is a universal B/T -scaling function where c_0 (constant residual resistivity extrapolated to $T = B = 0$); c_1 , and ζ are considered as fitting parameters, and γ is fixed by high magnetic field ($\mu_B B \gg k_B T$) slope $\partial\rho/\partial B$.

To identify a possible common microscopic mechanism for the T -linear and B -linear Planckian behaviors in cuprates,

we propose here a recently developed theoretical framework based on Kondo-like charge fluctuations near local quantum criticality of heavy-fermion formulated slave-boson t - J model [18]. This approach is motivated by the striking similarity in strange metal phenomenology between cuprates and heavy-fermion Kondo lattice systems, in which the Fermi surface volume reconstructs over the entire strange metal region in both systems. Therein, the electron is effectively fractionalized into charge-neutral fermionic spinon and a spinless charged holon (slave-boson). The hopping t -term is mapped onto a Kondo-like coupling where disordered slave boson interacts with fermionic spinon band and the effective conduction electron band made of spinon-holon bound fermion living on the bonds connecting nearest-neighbor sites (see Appendix A). The charge Kondo hybridization is dictated by the condensation of slave-boson. The antiferromagnetic Heisenberg exchange coupling J term is decomposed into Resonating-Valence-Bond spin liquid singlets in both spinon hopping and preformed d -wave Cooper pairing channels. Via a controlled perturbative renormalization group (RG) approach, the Planckian metal phase appears as a result of local disordered bosonic charge Kondo fluctuations coupled to a fermionic spinon band and a heavy hole-like spinon-holon bound fermion band near the Kondo-breakdown local quantum critical point (QCP) due to the competition between the pseudogap phase (dominated by the Heisenberg J term) and Fermi liquid (FL) phase (dominated by hopping t -term). It was further shown in Ref. [18] via RG renormalized 2nd-order perturbation in the hopping (effective Kondo) term that close to the predicted QCP an exact cancellation of the hopping coupling constant (t -term) in the self-energy of the fermionic spinons, spinon-holon bound fermions and slave-bosons occurs (see Appendix A and Appendix B). This leads to a universal local electron self-energy insensitive to couplings (or hole doping), reminiscent of but distinct from the Marginal-Fermi-Liquid (MFL) self-energy [18]. This further leads to an extended coupling-constant independent (doping insensitive) quantum critical strange metal "phase" showing a universal Planckian scattering rate with quantum-critical ω/T -scaling (see below).

This approach offers an excellent description of the quantum critical Planckian metal phase observed in cuprates [18], including: universal Planckian scattering rate in DC-transport over an extended doping range [8], bad metallic behavior with T -linear resistivity beyond MIR limit [19], universal quantum critical ω/T -scaling in optical (AC) conductivity and scattering rate [3], the marginal Fermi-liquid (MFL) spectral function observed in ARPES [20] as well as Fermi surface reconstruction observed in Hall coefficients in various overdoped cuprates [4, 10].

At a zero field in the Planckian metal phase, the conduction electron shows universal (coupling-constant independent) MFL-like self-energy: $\Sigma_c''(\omega, T \rightarrow 0) = -\frac{1}{\pi}|\omega|$. Via the general relation between self-energy and scattering rate: $1/\tau = -2\Sigma''$ and conformal transformation, the conduction electron self-energy at $T = 0$ leads to the finite-temperature AC-scattering rate with universal quantum critical ω/T -scaling: $\hbar/\tau(\omega, T) = \frac{2}{\pi}x \coth \frac{x}{4}$ with $x \equiv \hbar\omega/k_B T$, which in the static

limit gives the universal T -linear Planckian scattering rate: $\hbar/\tau(\omega \rightarrow 0, T) = \alpha_T k_B T$ with $\alpha_T = 8/\pi$ [18, 21]. At a finite field, the longitudinal magneto-conductivity via Drude formula is defined as: $\sigma_{xx} = \sigma_{yy} = (ne^2\tau_B/m^*)[1/(1 + (\omega_c\tau_B)^2)]$, where $\omega_c = eB/m^*$ is the cyclotron frequency. It was found experimentally that $\omega_c\tau_B \ll 1$ in the strange metal region of cuprates [22–24], the magnetic field effect is dominated by the Zeeman spin splitting of the fermionic bands; As a result, the Landau level and orbital motion of electrons are negligible, justifying the assumption of our approach. The longitudinal magneto-resistivity therefore takes the approximate Drude form: $\rho_{xx} \equiv \rho(B, T) \approx (m^*/ne^2)(1/\tau_B)$. We now generalize this approach by including the Zeeman term in magnetic field and focus on critical charge fluctuations near local criticality (Appendix A). Here, we restrict ourselves to the isotropic scattering where only the isotropic conduction electron states near the Fermi surface are considered (Fig. 3 Inset). At zero field, this approximation is further justified and supported by the experimental observation that the Planckian scattering rate is contributed from the isotropic component of scattering rate [25]. At a finite field, the Zeeman splitting effect will contribute to the isotropic component of the magneto-scattering rate. We obtain the AC magneto-scattering rate $1/\tau(\omega, B, T)$ by computing the field-dependent electron self-energy $\Sigma_c''(\omega, B, T)$. We find that the effect of Zeeman field on the fermionic self-energy $\Sigma_{\text{fermion}}^\sigma(\omega, B)$ is equivalent to a shift in fermionic frequency ω in the zero-field self-energy $\Sigma_{\text{fermion}}^\sigma(\omega)$: $\Sigma_{\text{fermion}}^\sigma(\omega, B) = \Sigma_{\text{fermion}}^\sigma(\omega \rightarrow \omega - s_\sigma \mu_B B)$, which applies to both fermionic spinons and spinon-holon bound fermions (see Appendix B). At a finite field, our model leads to the field- and spin-dependent AC magneto-scattering rate (after subtracting the purely T -dependent scattering rate $\hbar/\tau_0(T)$) as (see Appendix B):

$$\frac{\hbar}{\tau_B^\sigma} - \frac{\hbar}{\tau_0(T)} = \frac{2}{\pi} k_B T \left[\frac{\hbar\omega/2 + s_\sigma \mu_B B}{k_B T} \right] \coth \left[\zeta \frac{\hbar\omega/2 + s_\sigma \mu_B B}{2k_B T} \right] \quad (2)$$

with $s_\sigma = \text{sgn}(\sigma) = +1(-1)$ for $\sigma = \uparrow(\downarrow)$, respectively. Here, a tuning parameter ζ , allowed by conformal mapping of scattering rate in the scaling regime from zero temperature to finite temperatures [21] (see Appendix B, E), is introduced to match the observed universal B/T -scaling in magneto-scattering rate (see Eq. (1) and Fig. 1), whose value is constrained by the T -linear Planckian coefficient $\alpha_T = 8/\pi$ (see below and Appendix B, C).

The total field dependent magneto-scattering rate (subtracted by a constant residual scattering rate at $\omega = B = T = 0$) is given by $\hbar/\tau_B - \hbar/\tau_0(T) = \hbar/\tau_B^\uparrow + \hbar/\tau_B^\downarrow$, where $\hbar/\tau_0(T) = bk_B T$ with $b = 8(1 - 1/\zeta)/\pi$ being the T -linear residual scattering rate at $\omega = B = 0$. In the DC ($\omega \rightarrow 0$) limit, this gives universal B/T -scaling in scattering rate

$$\frac{\hbar/\tau_B - \hbar/\tau_0(T)}{k_B T} = \frac{2}{\pi} \frac{\mu_B B}{k_B T} \coth \left(\zeta \frac{\mu_B B}{2k_B T} \right). \quad (3)$$

The universal scaling function in scattering rate (Eq. (3)) from which Eq. (1) is deduced, is our key theoretical result.

Remarkably, as we will show in the following section, it unifies the T -linear and B -linear Planckian strange metal state in magneto-resistivity observed in cuprates: (i) It gives excellent analytic fits (within error bars) to the observed T -linear and B -linear Planckian scattering rates in the zero field and zero temperature limit, respectively: $\hbar/\tau_B(B=0, T) = \alpha_T k_B T$ with $\alpha_T = 8/\pi$ and $\hbar/\tau_B(B, T=0) = \alpha_B \mu_B B$ as well as the correlation between them $\alpha_B = \alpha_T/2 = 4/\pi$ (Fig. 3); (ii) More generally at finite temperatures and fields, it leads to the universal scaling function $f(x)$ well fitted to $\rho(B, T)$ in Fig. 1 and $d\rho/dB$ in Fig. 2. The scaling function based on Eq. (1) and Eq. (3) further undermine the Marginal Fermi Liquid (MFL) assumption [26] (see Fig. 9 in Appendix C), with empirical quadrature scaling form $\rho - \rho_0 \sim \sqrt{(ak_B T)^2 + (b\mu_B B)^2}$. This formula for MFL does not allow for a regime in which T -linear and B -linear resistivity co-exist, which is the most striking feature of the data for $T < 50$ K and $B > 60$ T. (indicated by the shaded regions in Fig. 1).

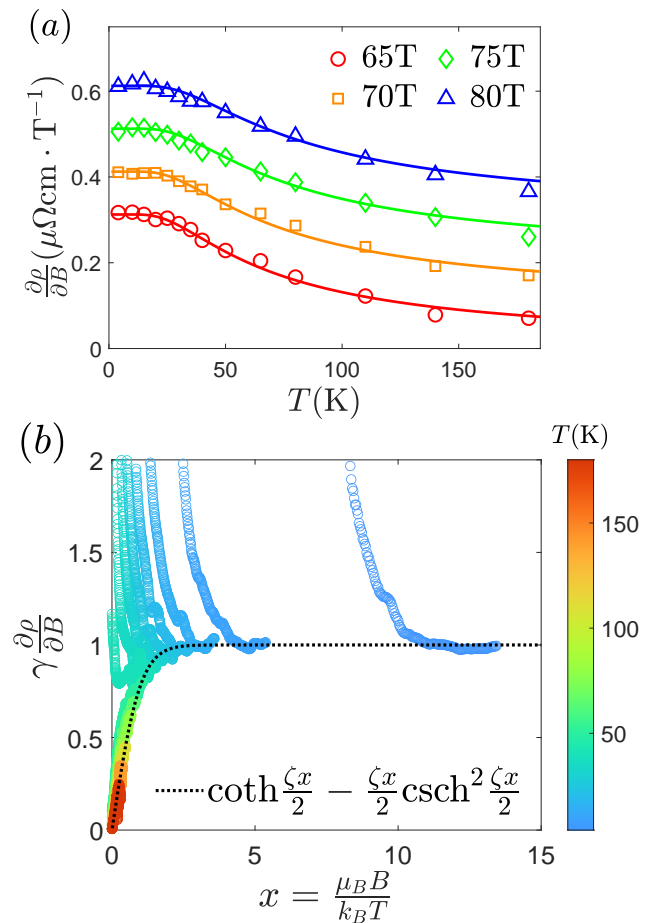


Figure 2. (a) Slope of the magneto-resistivity with respect to magnetic field versus temperature at different magnetic fields for doping $p = 0.19$. Colored symbols represent experimental data and colored solid lines correspond to the associated theoretical prediction [Eq. (C19)] obtained by taking the derivative of Eq. (1), with same parameter values as in Fig. 1 : $\gamma = 3.2(\mu\Omega\text{cm})^{-1}\text{T}$, $\zeta = 3.06$. For visibility, the data points and curves have been shifted by $0.1\mu\Omega\text{cm} \cdot \text{T}^{-1}$ in the y-axis successively for each value of magnetic field. (b) B/T -scaling of the rescaled slope of the magneto-resistivity as a function of $x = \mu_B B / (k_B T)$ for doping $p = 0.19$. The slope values are then rescaled by $\gamma_{p=0.19} = 3.2(\mu\Omega\text{cm})^{-1}\text{T}$ for $p = 0.19$, such that at high magnetic field values $\mu_B B \gg k_B T$, the product $\gamma(\partial\rho/\partial B)$ saturates to unity. Note that γ depends on the carrier density n and is expected to slightly vary for different doping values. The black dotted line corresponds to the theoretical prediction of the derivative of the magneto-resistivity given in Eq. (C19) with $\zeta = 3.06$. Magneto-resistivity data are reproduced from the same data as in [9] for $p = 0.19$.

III. FITTING THE DATA WITH THE THEORETICAL FRAMEWORK

The form of Eq. (1) is derived from a recently developed theoretical framework based on Kondo-like charge fluctuations near a local quantum critical point within the slave-

p	c_0 ($\mu\Omega\text{cm}$)	c_1 ($\mu\Omega\text{cm/K}$)	ζ	γ (T/ $\mu\Omega\text{cm}$)
0.19	6.48	0.685	3.06	3.2

Table I. The fitting parameters used for the LSCO $p = 0.19$ data throughout the manuscript. The values of c_1 and γ can be calculated from the theory and agree well with these values (see Table (II) of the Appendix C2).

boson formulation of the t - J model [18], as explained in detail in the previous section. This framework naturally accounts for a unified microscopic origin of the T -linear and B -linear Planckian behaviors in cuprates (see Section II, Appendix B).

As shown in Fig. 1, magneto-resistivity both in the T -linear (Fig. 1 (a)) and B -linear (Fig. 1 (b)) limits are well fitted by Eq. (1); and B/T -scaling behavior is clearly seen in $[\rho(B, T) - \rho_0(T)]/T \propto \Phi(x)$ (Fig. 1 (c)). It is important to note that we use the same values of these four fitting parameters for all fits for $p = 0.19$ throughout the manuscript (see Table (I)).

At fixed higher fields, the seemingly two T -linear behaviors of magneto-resistivity observed at lower and higher temperature regions (Fig. 1 (a)) can be well accounted for by Eq. (1) as a result of interplay between T -linear term $\rho_0(T)$ and the scaling function $\Phi(x)$ (see Fig. 17 in Appendix D). Meanwhile, in Fig. 1 (b), the deviation between theoretical predictions (dashed lines) and the data at low temperatures is likely due to superconducting fluctuations. Such a deviation vanishes at a higher temperature well above T_c (see the fit to $T = 180\text{K}$ data), where superconducting fluctuations are absent. Moreover, the B/T -scaling function $\Phi(x)$ can be extracted directly by taking the slope of the magneto-resistivity $d\rho/dB$. As shown in Fig. 1 (c), clear universal B/T -scaling exists in the slope of magneto-resistivity, which is a signature of quantum criticality. We further find this quantum critical behavior exists over an extended doping (p) range $0.16 < p < 0.19$: $\gamma d\rho/dB = f(x)$, where $f(x) = \coth(\zeta x/2) - \zeta x \operatorname{csch}^2(\zeta x/2)$ is a universal well-fitted scaling function with $\zeta \approx 3.06$ (see Fig. 2 and Fig. 8) [9, 18]. The temperature dependent slope of magneto-resistivity $\partial\rho(B, T)/\partial B$ observed in Ref. [9] is also well-fitted by $f(x)$, coming from the same scaling function $\Phi(x)$ (Fig. 2 (a)) for $\partial\rho/\partial B$ vs. T at different fields, and Fig. 2 (b) for $\gamma d\rho/dB$ vs. x . Similar results have been reported in other cuprate compounds [10]. Note that the normalized scaling function $f(x)$ is identical to that for AC-scattering rate found in Ref. [18] provided $x \equiv \hbar\omega/k_B T$ and $\hbar\omega \equiv 2\zeta\mu_B B$.

IV. CORRELATION BETWEEN CO-EXISTING T -LINEAR AND B -LINEAR PLANCKIAN SCATTERING RATES NEAR OPTIMAL DOPING

The T -linear Planckian scattering rate for LSCO in Ref. [9] in the quantum critical scaling regime was recently studied in Ref. [8]. Therein, the doping insensitive Planckian coefficient $\alpha_T \sim 2.6$ (for $0.16 < p < 0.19$) was found from the zero-field T -linear resistivity in the SM region via the

Drude formula expressed in terms of plasma frequency (ω_p) (Fig. 1 (a)): $\rho(T, B = 0) = A_T^1 T = (4\pi/\omega_p^2)(1/\tau) = (m^*/ne^2)(1/\tau)$ with $\omega_p^2 = 4\pi ne^2/m^*$ [27], m^* being electron effective mass, and $1/\tau = \alpha_T k_B T/\hbar$ being the Planckian scattering rate. Here, n/m^* ratio is directly estimated via the plasma frequency through optical conductivity data as: $\omega_p^2 \approx 4\pi e^2 a_w p/V m_e$ with $a_w \sim 0.42$ [3, 8, 28, 29], $V = Al$ is the volume of unit cell with $A = a^2$ being the planar area, $a \simeq 0.378\text{ nm}$ being the in-plane lattice spacing, and $l \simeq 0.66\text{ nm}$ being the CuO_2 interlayer distance.

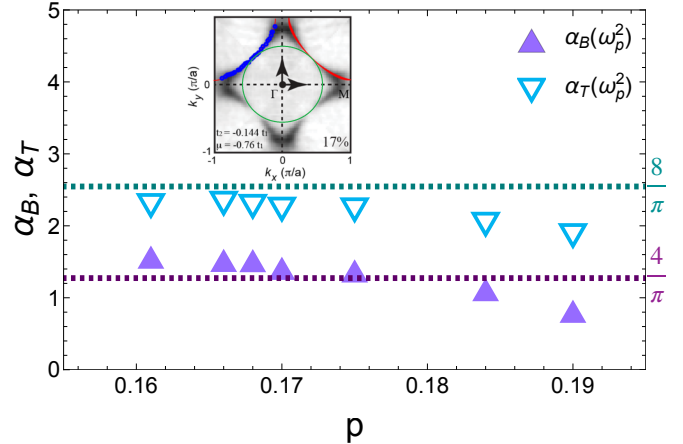


Figure 3. The linear-in-temperature (down triangles) and linear-in-field (up triangles) Planckian coefficients versus doping for LSCO obtained from magneto-resistivity data reproduced from Ref. [9] as detailed in Appendix D. Horizontal purple and turquoise dashed lines correspond to theoretical prediction $\alpha_T = 8/\pi \simeq 2.54$ and $\alpha_B = 4/\pi \simeq 1.27$, respectively. Note that our theoretical framework finds quantitative agreement with the experimentally measured values of α_B and agrees within $\sim 25\%$ of the experimentally measured values of α_T . The calculated ratio of $\alpha_T/\alpha_B = 2$ is in close agreement with experimental data for $0.16 < p < 0.19$. Inset: A plot of two-dimensional Fermi surface of LSCO at $p = 0.17$ (dark region guided by red and blue curves), as measured by ARPES and adapted from Ref. [30]. The green circle is a schematic plot of isotropic electronic states near the Fermi surface that contribute to the isotropic scattering rate within our theoretical framework in the experimental doping range $0.16 < p < 0.19$.

We examine whether the similar Planckian behavior exists in the B -linear magneto-resistivity in the same doping of the same material (LSCO) studied in Ref. [9]. We first extract the slope A_B^1 of the low-temperature (averaged between $T = 20\text{K}$ and $T = 30\text{K}$) linear-in-field magneto-resistivity: $\rho(B, T = T_0) - \rho_0 = A_B^1 B$. Via the Drude form of $\rho(B, T)$, we indeed find the similar doping-insensitive universal Planckian behavior in magneto-transport of the same compound in the same doping range $\hbar/\tau_B = \alpha_B \mu_B B$ with the Planckian coefficient $\alpha_B = \hbar(\omega_p^2/4\pi)A_B^1/\mu_B = \hbar(ne^2/m^*)A_B^1/\mu_B \sim 1.4$ (with the same m^* and n as those at zero field) (Fig. 3). Remarkably, we find the two Planckian coefficients α_T, α_B are correlated by the approximated relation: $\alpha_T \sim 2\alpha_B$, emerging from the correlation between the slopes of T -linear and B -linear resistivities: $A_T^1 \sim 2A_B^1$ [9]. Similar correlation be

tween A_T^1 and A_B^1 slopes was observed in the strange metal state of different cuprate compounds [11].

Note that plasma frequency approach from optical conductivity measurement is an accurate and reliable approach to estimate the Planckian coefficients α_T and α_B since it gives directly the needed n/m^* ratio. Though the error bars in determining α_T and α_B is increased, m^* and n can also be estimated separately where $m^* \sim 1/p$ is obtained from specific heat and $n \sim n_{eff} \sim 1/V$ [8]. As shown in Fig. 20, we find that the values of α_T and α_B estimated from both approaches agree very well. Here, the carrier density n is taken as an effective density n_{eff} by fitting to $\omega_p^2 \propto n/m^* \propto p$ with $m^* \sim 1/p$ [8] (see Appendix D). To reconcile the discrepancy between the doping insensitive $n_{eff} \sim 1/V$ estimated here and the doping dependent carrier density n via the Hall coefficient measurement goes beyond the scope of the present work and deserves further study elsewhere.

V. DISCUSSIONS

Within our theoretical framework, we find in 2D limit the fitting parameters γ and c_1 , as defined in Eq. (1), take the analytical forms: $\gamma_{2D} = (\hbar n e^2)/(m^* \alpha_B \mu_B)$ and $c_1 = (m^*/n e^2)(k_B/\hbar)(\alpha_T - \alpha_B/\zeta)$. Their values obtained via the above analytic forms (see Appendix C 2) are in good agreement with that by numerical fits in Fig. 1 and Fig. 2.

Since in the quantum critical state the thermal energy is the only relevant energy scale, ω/T -scaling in observables can be in general understood as the universal scaling in the dimensionless ratio between the external energy ($\hbar\omega$) and the thermal energy ($k_B T$). In this context, the B/T -scaling in cuprates is expected from the ω/T -scaling since the Zeeman-energy from external magnetic fields ($\mu_B B$) constitutes one possible realization of the external energy in the quantum critical state. Note that our mechanism based on Zeeman splitting predicts that the Planckian scattering rate $1/\tau_B$ is insensitive to field orientation, as observed in Ti2201 and Bi2201 [10]. However, clear field-angle dependence of magneto-resistivity has been observed in the overdoped region ($p = 0.23, 0.24$) of LSCO, possibly due to proximity of Fermi surface to the Van Hove singularity at those dopings [14, 31]. This could explain the deviation of our theoretical predictions for α_T , α_B from the experimentally observed values (Fig. 3) as p increases. In this case of proximity to the Van Hove singularity, a correction to our analysis from the anisotropic orbital motion is to be expected, which goes beyond the scope of this paper.

Our experimental and theoretical analysis strongly supports the scenario of a quantum critical point (QCP) hidden inside the superconducting dome in cuprates. It separates pseudogap from Fermi liquid phases and serves as a common origin of the observed T -linear and B -linear resistivity. We anticipate this QCP to emerge at $B = B_c \sim 60$ T [32, 33], $p = p_c \sim 0.19$ and $T \rightarrow 0$ where superconductivity is suppressed exactly by field near critical (optimal) doping, in LSCO. As shown in Fig. 4, based on existing data and our theory, we propose a quantum critical fan-like volume, expanded from the single QCP in the general doping-field-temperature (p, B, T) phase

diagram of LSCO, serving as a common origin to unify the universal T -linear and B -linear Planckian scattering rate as well as B/T -scaling in magneto-resistivity observed therein. Further experimental studies are needed to clarify this picture.

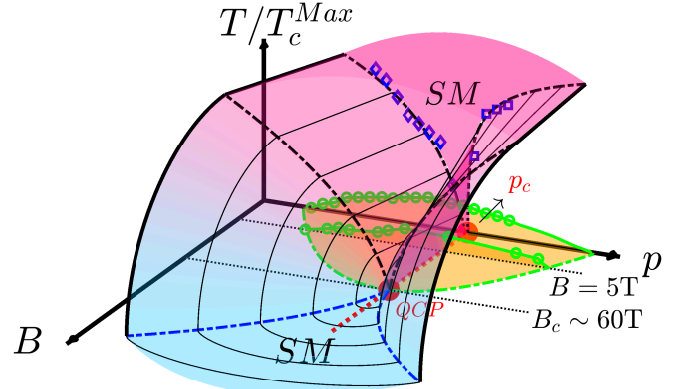


Figure 4. The doping-field-temperature (p, B, T) phase diagram of LSCO near critical doping $p_{cr} \sim 0.19$ based on magneto-transport data in [9]. Green circles defining the superconducting T_c dome are experimental data obtained from [24] at zero magnetic field, and from [34] for finite magnetic field $B = 5$ T. Blue diamonds and blue square are data from [8] and [24] respectively and correspond to the crossover temperature between the SM phase into the PSG phase and the FL phase. Note that the temperature axis is rescaled by T_c^{Max} , which is experimental group dependent, and is defined by the highest T_c value of superconducting T_c dome at zero field.

Acknowledgments. This work is supported by the National Science and Technology Council (NSTC) Grants 110-2112-M-A49-018-MY3, the National Center for Theoretical Sciences of Taiwan, Republic of China (C.H.C.). C.H.C. acknowledges the hospitality of Aspen Center for Physics, USA and Kavli Institute for Theoretical Physics, UCSB, USA where part of the work was done. This research was supported in part by grant NSF PHY-2309135 to the Kavli Institute for Theoretical Physics (KITP). The experimental data in this paper were collected at the NHMFL, supported by the NSF through DMR-1644779.

Appendix A: Methods

Our starting point is the heavy-fermion formulated slave-boson t - J (HFSBtJ) Hamiltonian on 2D lattice which was developed recently [18, 35]. We start from the original one-band t - J model, reads:

$$H_t = -t \sum_{\langle i,j \rangle, \sigma} c_{i\sigma}^\dagger c_{j\sigma} - \mu \sum_{i\sigma} c_{i\sigma}^\dagger c_{i\sigma},$$

$$H_J = J_H \sum_{\langle i,j \rangle} \mathbf{S}_i \cdot \mathbf{S}_j, \quad (A1)$$

where (t, μ, J_H) denotes the (hopping strength, chemical potential, Heisenberg coupling). Under the slave-boson representation $c_{i\sigma}^\dagger \rightarrow f_{i\sigma}^\dagger b_i$ with $f_{i\sigma}$ (b_i) being fermionic charged-neutral spinon (bosonic spinless charged holon) operators, the

hopping t -term is mapped via Hubbard-Stratonovich transformation onto a Kondo-like coupling where disordered slave boson (holon b -field) interacts with fermionic spinon (f -field) band and the effective conduction electron band made of spinon-holon bound fermion (ξ -field with $\xi_{ij}^\sigma = \sum_{\langle i,j \rangle} b_i f_j^\sigma$) living on the bonds connecting nearest-neighbor sites $\langle i, j \rangle$ [35, 36]

$$H_t \rightarrow \frac{t}{\sqrt{N}} \sum_{\langle i,j \rangle, \sigma} \left[\left(f_{i\sigma}^\dagger b_j^\dagger + f_{j\sigma}^\dagger b_i^\dagger \right) \xi_{ij, \sigma} + H.c. \right]. \quad (\text{A2})$$

The charge Kondo hybridization is dictated by the condensation of slave-boson. The anti-ferromagnetic Heisenberg exchange coupling J term is decomposed into Resonating-Valence-Bond (RVB) spin liquid singlets in both particle-hole ($\chi_{ij} = \chi = \langle f_{i\sigma}^\dagger f_{j\sigma} \rangle$) and particle-particle (d -wave Cooper pairing $\Delta_{ij} = \Delta = \langle f_{i\uparrow}^\dagger f_{j\downarrow}^\dagger - f_{j\uparrow}^\dagger f_{i\downarrow}^\dagger \rangle$) channels

$$\begin{aligned} H_J \rightarrow & -J_H \sum_{\langle i,j \rangle} \left(\sum_{\sigma} \chi_{ij} f_{i\sigma}^\dagger f_{j\sigma} + H.c. - |\chi_{ij}|^2 \right) \\ & + J_H \sum_{\langle i,j \rangle} \sum_{\sigma, \sigma'} \left(\Delta_{ij} \varepsilon_{\sigma\sigma'} f_{i\sigma}^\dagger f_{j\sigma'}^\dagger + H.c. \right) \\ & + J_H \sum_{\langle i,j \rangle} |\Delta_{ij}|^2. \end{aligned} \quad (\text{A3})$$

Four mean-field phases are realized depending on whether Bose-condensation of the slave-boson b -field $\langle b_i \rangle = \langle b \rangle$ and Δ -field $\langle \Delta \rangle$ occurs: the pseudogap phase, known as Z_2 fractionalized FL or Z_2 FL* [37] (Landau Fermi liquid, FL) is reached when $\langle \Delta \rangle \neq 0$, $\langle b \rangle = 0$ ($\langle \Delta \rangle = 0$, $\langle b \rangle \neq 0$); while the $U(1)$ FL* (d -wave superconducting) phase arises when $\langle b \rangle = \langle \Delta \rangle = 0$ ($\langle b \rangle \neq 0$, $\langle \Delta \rangle \neq 0$). The Planckian metal phase appears in $U(1)$ FL* phase beyond mean-field as a result of critical local charge Kondo fluctuations where disordered local bosons couple to a fermionic spinon band and a heavy-electron band near a localized-delocalized quantum critical point due to the competition between the pseudogap phase (dominated by J) and FL phase (dominated by t).

The action of the model at zero field beyond mean-field in $U(1)$ FL* is given by Ref. [18]. We shall explore the phase diagram in $U(1)$ FL* phase beyond mean-field by including fluctuations of both t - and J -terms. We will not include $U(1)$ gauge fluctuations in our RG analysis since the spinons are deconfined and stable against them due to the presence of a spinon Fermi surface [38]. The leading effective action in units of the half-bandwidth of the f -spinon band $D \approx 4\chi \approx 4J_H$ beyond the mean-field level reads

($\hbar = k_B = 1$) [18]

$$\begin{aligned} S = & - \sum_{k\sigma} f_{k\sigma}^\dagger \mathcal{G}_f^{-1}(k) f_{k\sigma} - \sum_k b_k^\dagger \mathcal{G}_b^{-1}(k) b_k \\ & + \sum_{k\sigma a} \xi_{k\sigma}^{a\dagger} \mathcal{G}_\xi^{-1}(k) \xi_{k\sigma}^a + \sum_{ka} \varphi_k^{a\dagger} \mathcal{G}_\varphi^{-1}(k) \varphi_k^a \\ & + \frac{g}{\sqrt{\beta N_s}} \sum_{kp\sigma a} \left(f_{k\sigma}^\dagger b_p^\dagger \xi_{k+p, \sigma}^a + H.c. \right) \\ & + \frac{J}{\sqrt{\beta N_s}} \sum_{kp a} \left[f_{k\uparrow}^\dagger f_{p\downarrow}^\dagger \varphi_{k+p}^a + H.c. \right] \end{aligned} \quad (\text{A4})$$

with $k = (\mathbf{k}, \omega)$ and $p = (\mathbf{p}, \nu)$, φ being the fluctuating field for the d -wave RVB pairing order parameter Δ . In the phases with $\langle b \rangle = 0$, the bare hopping parameter t is strongly suppressed by the disordered bosons, leading to an effective hopping $g \equiv 2t\sqrt{\delta}$. Here, $J = 2J_H$ is the effective exchange, $\mathcal{G}_f(k) = (i\omega - \varepsilon_{\mathbf{k}})^{-1}$, $\mathcal{G}_\xi(k) = \zeta^{-1} (i\omega - \xi_{\mathbf{k}})^{-1}$, $\mathcal{G}_b = (i\omega - \lambda)^{-1}$, and $\mathcal{G}_\varphi = (J/2)^{-1}$ denote the bare Green's functions (see Appendix B in Ref. [18]). The momenta relevant for the bosonic φ field are near the antinode. Our perturbative expansion in bare couplings g , J is controlled since $g/D, J/D < 1$ (for an estimated $J_H/t \sim 0.3$). To study the charge dynamics and transport properties, we go beyond static mean-field level of ξ field by generating its dynamics and dispersion via second-order hopping process at fixed $g = g_0^*$ such that $\zeta^{-1} \equiv (g^2 \rho_0/D)^{-1}$ appears as a prefactor in \mathcal{G}_ξ , with $\rho_0 = 1/D$ being the constant density of states at Fermi level for f spinon band. The f -spinon band is approximated by a linear-in-momentum dispersion, namely $\varepsilon_{\mathbf{k}} = h_{\mathbf{k}} - \mu_f \approx v|\mathbf{k}|$ with $h_{\mathbf{k}} \equiv -2\chi(\cos k_x + \cos k_y)$ and $\mu_f = \mu - \lambda$ being the effective chemical potential for f spinon (μ is the chemical potential for the original conduction electron, see Appendix A in Ref. [18]). Here, the spinon band is fixed at half-filling, $\mu_f = 0$. The band structure for the ξ fermion shows a hole-like dispersion, $\xi_{\mathbf{k}} = -\zeta \varepsilon_{\mathbf{k}} - \mu_\xi$. The Lagrange multiplier $\lambda > 0$ is introduced to enforce the local constraint for slave boson. The slave boson (b field) is effectively treated as a local boson with a flat band of energy λ and with a negligible dispersive band (see Appendix B in Ref. [18]). In the pseudogap and $U(1)$ FL* phases, the chemical potential of the ξ band μ_ξ fixes hole doping δ for the system such that $N_s^{-1} \sum_{ij, \sigma} \langle \xi_{ij, \sigma}^\dagger \xi_{ij, \sigma} \rangle = \delta$. Our model in Eq. (A4) shows the $U(1)$ gauge symmetry: $f_{i\sigma} \rightarrow f_{i\sigma} e^{i\theta_i}$, $b_i \rightarrow b_i e^{i\theta_i}$, $\chi_{ij} \rightarrow \chi_{ij} e^{i(\theta_i - \theta_j)}$ and $\xi_{ij, \sigma} \rightarrow \xi_{ij, \sigma} e^{i(\theta_i + \theta_j)}$.

In Ref. [18], the one-loop perturbative renormalization group (RG) analysis was applied to study the quantum phase transition of the action (Eq. (A4) and Fig. 2 in Ref. [18]) due to competition between charge fluctuations of the hopping t (effective Kondo) term and the RVB fluctuations (the J term). It is convenient to define the dimensionless bare coupling constants $g \rightarrow g/D$, $J \rightarrow J/D$, and absorb $1/\zeta$ in \mathcal{G}_ξ into g by a rescaling, $g \rightarrow \bar{g} = g/\sqrt{\zeta}$, $\xi \rightarrow \sqrt{\zeta} \xi$. Our RG analysis is perturbatively controlled as $\bar{g} < 1$ (the bare value $g < g_0^*$ is set), and $J < 1$. Our RG approach can be further controlled by the ϵ -expansion technique with a small parameter $\epsilon = d - z$ within the convergence radius $|\epsilon| \leq 1$. We set the dynamical

exponent $z = 1$ due to the linearized dispersion of f , and spatial dimension $d = 2$ here.

Following the above RG approach, a non-trivial quantum critical point (QCP) was predicted, separating all the above-mentioned four mean-field phases (U(1) FL*, pseudogap, superconducting and FL phases). In the strange metal state with $\langle b \rangle = \Delta = 0$, the gauge-invariant (physical) electron operator can be constructed from ξ_{ij} and φ_{ij} as $c = \xi\sqrt{2}\varphi_{ij}^*\sqrt{J}$. The dynamical scattering (relaxation) rate at $T = 0$ is calculated via the imaginary part of the electron self-energy: $\tau(\omega) = -\hbar/2\Sigma_c''(\omega)$ and $\Sigma_c''(\omega) = (1/2)\Sigma_\xi''(\omega)$, where $\Sigma_\xi''(\omega)$ at $T = 0$ is obtained via RG renormalized second-order perturbation close to the QCP, where the bare couplings are replaced by the renormalized ones i.e. $\bar{g}, \bar{g}_0^* \rightarrow \bar{g}(l)$ with $l \equiv -\ln(\bar{D}) > 0$ being the RG running cutoff length scale and $\bar{D} < D$ being the RG running cutoff energy scale [18]. As a result, close to the predicted QCP an exact cancellation of the coupling constant g in the self-energy $\Sigma_{f/\xi}$ occurs between $1/g^2$ in G_ξ and g^2 in the corresponding Feynman diagram of the self-energy, i.e. the coupling constant dependence of the prefactor g^2/ζ in $\Sigma_{f/\xi}$ gets exactly cancelled under RG: $g^2/\zeta \rightarrow D^2\bar{g}^2(l)/\bar{g}^2(l) \rightarrow D^2$ (see Eq. (B1) in Appendix B and Fig. 5). This leads to a universal local Marginal-Fermi-Liquid-like self-energy insensitive to couplings, including a constant and a linear-in- $|\omega|$ term, i.e. $\Sigma_\xi''(\omega) = \alpha - \zeta|\omega|$ with $\alpha \approx \frac{5}{2}\bar{g}^2\rho_0 = \frac{5}{2}D$ and $\zeta = \frac{2}{\pi}$; and further leads to a coupling-constant independent Planckian scattering rate with universal quantum-critical ω/T -scaling [18] (see the main text). This Planckian metal state becomes a quantum critical "phase", extending to the entire U(1) FL* phase, in excellent agreement with universal Planckian scattering rate observed in cuprates in DC-transport over an extended doping range [8].

We now generalize Eq. (A4) in magnetic fields by including a Zeeman term as

$$S(B) = S(B = 0) + H_B \quad (\text{A5})$$

with $S(B = 0) = S$ given by Eq. (A4) and H_B being a Zeeman Hamiltonian

$$H_B = -\mu_B B_z \sum_k \left[\left(f_{k\uparrow}^\dagger f_{k\uparrow} - f_{k\downarrow}^\dagger f_{k\downarrow} \right) + \left(\xi_{k\uparrow}^\dagger \xi_{k\uparrow} - \xi_{k\downarrow}^\dagger \xi_{k\downarrow} \right) \right]. \quad (\text{A6})$$

With Eq. (A6) included, the energies of the f -spinon band (ϵ_f) and ξ -fermion band (ϵ_ξ) are shifted by the Zeeman energy: $\epsilon_{f,\xi}^\sigma \rightarrow \epsilon_{f,\xi}^\sigma - s_\sigma \mu_B B$ with $s_\sigma = \pm 1$ for spin-up and spin-down fermion, respectively.

Appendix B: Magneto-scattering rate for conduction ξ -band and physical c -electron band

In this section, following RG renormalized second-order perturbation in Ref. [18], we calculate the magneto-scattering rate for conduction ξ -band and the corresponding physical c -electron band by computing the local self-energy of the ξ -fermions near local quantum criticality. Here, we restrict our-

selves to the isotropic scattering where only the isotropic conduction electron states near the Fermi surface are considered (Fig. 3 Inset). At zero field, this approximation is further justified and supported by the experimental observation that the Planckian scattering rate is contributed from the isotropic component of scattering rate [25]. At a finite field, the Zeeman splitting effect will contribute to the isotropic component of the magneto-scattering rate. The local self-energy of the ξ field is given by (see Fig. 5)

$$\begin{aligned} \Sigma_\xi(ik_n) &= \left(\frac{g^2}{N_s \zeta \beta} \right) \frac{1}{2} \sum_{p,\sigma} G_f^\sigma(p) G_b(k-p) \\ &\approx \left(\frac{g^2}{\zeta \beta} \right) \sum_{ip_m} \left(\frac{1}{N_s} \sum_p G_f(p) \right) \mathcal{G}_b(k-p), \quad (\text{B1}) \end{aligned}$$

where G_f denotes the self-energy corrected Green's function of f -spinon and \mathcal{G}_b stands for the bare Green's function of the slave-boson b -field; and the momentum and Matsubara frequency are defined via the compact notation $p \equiv (ip_m, \mathbf{p})$. Here, the slave-boson b -fields are initially (at the bare level) treated as local impurity-like boson fields with no Bose condensation. In the wide-band limit the narrow band of the b -fields ($\epsilon_b(k)$) perturbatively generated through self-energy correction is negligible ($\epsilon_b(k) \ll D, \lambda$), and under one-loop RG, the local self energy of the b -field $\Sigma_b(\omega)$ does not lead to logarithmic divergence in running cutoff scale ($\Sigma_b \propto [l]^0$) [18]. Therefore, within the one-loop RG scheme, the slave-boson Green's function is approximated as the bare Green's function \mathcal{G}_b in Eq. (B1). Note that as mentioned above, under RG, an exact cancellation of coupling constant dependence in $\Sigma_{\xi/f}$ occurs: $g^2/\zeta \rightarrow D^2\bar{g}^2(l)/\bar{g}^2(l) \rightarrow D^2$.

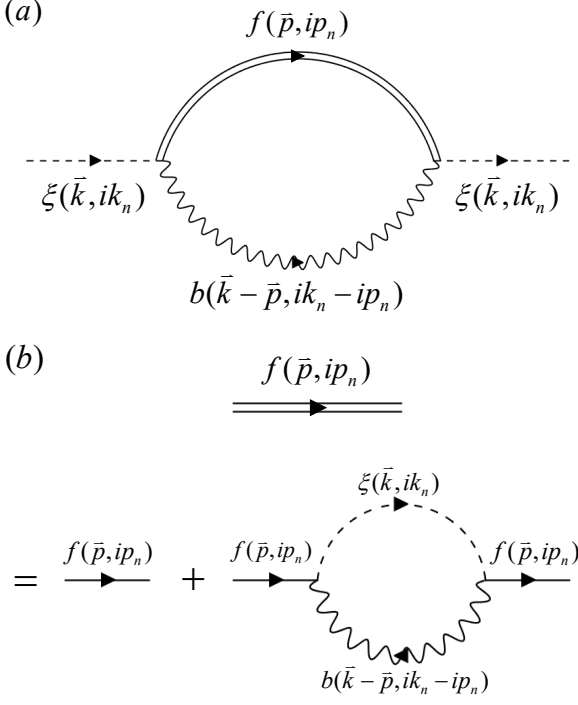


Figure 5. The self-energies (a) Σ_ξ and (b) Σ_f , where the solid lines represent the spinon fields G_f^σ , the dashed lines the slave-boson fields G_b , and the wavy lines the ξ -fermion fields G_ξ^σ .

Following perturbative analysis shown in Ref. [18], in the wide-band limit $D/\omega \gg 1$, the Zeeman splitting of the self-energies effectively leads to shifts of fermionic frequencies $\omega \rightarrow \omega + s_\sigma \mu_B B$ for both f -spinons and ξ -fermions.

To proceed with the calculation, we first compute the self-energy Σ_f^σ in G_f in Eq. (B1) as follows.

$$\Sigma_f^\sigma(k_n, k, B, \omega_n) = -\frac{g^2}{2N_s\beta} \sum_{p_n, p} \mathcal{G}_\xi(p_n, p, B) \mathcal{G}_b(p_n - \omega_n, p - k), \quad (\text{B2})$$

where $\mathcal{G}_\xi = \frac{1}{\zeta} \frac{1}{ip_n - (\epsilon_\xi(p) - \mu_\xi) - s_\sigma \mu_B B - i\Sigma_\xi''(p_n)}$ and $\mathcal{G}_b(p) = \frac{1}{ip_n - \lambda}$ are bare (initial) Green's functions of ξ -field and b -field, respectively, with $\zeta = g^2/D^2$, $\epsilon_\xi(p) - \mu_\xi = -(\epsilon_p - \bar{\mu}_\xi)$ with $\bar{\mu}_\xi = -\mu_\xi$, and $\Sigma_\xi''(p_n) = \pi D \operatorname{sgn}(p_n)$. Thus we obtain

$$\Sigma_f^\sigma(k_n, k, B, \omega_n) = -\frac{g^2}{2\zeta N_s\beta} \sum_{p_n, p} \frac{1}{ip_n - i\omega_n - \lambda} \times \frac{1}{ip_n + (\epsilon_p - \bar{\mu}_\xi) - s_\sigma \mu_B B - i\pi D \operatorname{sgn}(p_n)}. \quad (\text{B3})$$

Due to the sgn function in Σ_ξ'' , Eq. (B3) can be expressed as $\Sigma_f^\sigma = \Sigma_f^{>} + \Sigma_f^{<}$, where $\Sigma_f^{\sigma \gtrless}$ corresponds to $p_n \gtrless 0$ branch

in the Matsubara sum.

$$\begin{aligned} \Sigma_f^{\sigma \gtrless}(k_n, k, B, \omega_n) = & -\frac{g^2}{2\zeta N_s\beta} \sum_{p_n \gtrless 0} \sum_p \frac{1}{ip_n - i\omega_n - \lambda} \\ & \times \frac{1}{ip_n + (\epsilon_p - \bar{\mu}_\xi) - s_\sigma \mu_B B \mp i\pi D}. \end{aligned} \quad (\text{B4})$$

Following the analysis in Appendix E of Ref. [18], we have

$$\begin{aligned} \Sigma_f^{\sigma >} = & \frac{D^2 \rho_0}{2} \\ & \times \int_{-D + \bar{\mu}_\xi}^{D + \bar{\mu}_\xi} d\epsilon' \frac{n_F(\epsilon' + s_\sigma \mu_B B + i\pi D)}{i\omega_n - \epsilon' + \lambda - s_\sigma \mu_B B - i\pi D}, \end{aligned} \quad (\text{B5})$$

which in the $T \rightarrow 0$ limit becomes

$$\Sigma_f^{\sigma >} = \frac{D^2 \rho_0}{2} \int_{-D + \bar{\mu}_\xi + s_\sigma \mu_B B}^{s_\sigma \mu_B B} \frac{d\bar{\epsilon}}{i\omega_n - \bar{\epsilon} + \lambda - i\pi D}, \quad (\text{B6})$$

where $\epsilon' \equiv -\epsilon + \bar{\mu}_\xi$ and $\bar{\epsilon} \equiv \epsilon' + s_\sigma \mu_B B$. Note that under RG, $g^2/\zeta \rightarrow D^2 \bar{g}^2(l)/\bar{g}^2(l) \rightarrow D^2$. Performing the analytical continuation by absorbing λ into ω , $i\omega_n \rightarrow \omega - \lambda + i\eta$ for $\eta \rightarrow 0^+$, we get (in the $T \rightarrow 0$ limit)

$$\begin{aligned} & \left[\Sigma_f^{\sigma >}(\omega > 0) \right]'' \\ &= \frac{\pi D^2}{2} \int_{-D + \bar{\mu}_\xi + s_\sigma \mu_B B}^{s_\sigma \mu_B B} \frac{d\epsilon}{(\omega - \epsilon)^2 + (\pi D)^2} \\ &\equiv -\frac{1}{2\rho_0} \left[\frac{\omega - s_\sigma \mu_B B}{\pi D} - \tan^{-1} \frac{1}{\pi} \right] \\ &= \frac{\alpha}{2} - \frac{1}{2\pi} (\omega - s_\sigma \mu_B B), \end{aligned} \quad (\text{B7})$$

where $\alpha = D \tan^{-1} \frac{1}{\pi} \approx D/3$. Similarly, we find

$$\left[\Sigma_f^{\sigma <}(\omega < 0) \right]'' = - \left[\frac{\alpha}{2} - \frac{1}{2\pi} (\omega - s_\sigma \mu_B B) \right]. \quad (\text{B8})$$

Combining $\Sigma_f^{\sigma \gtrless}(\omega \gtrless 0)$, we obtain (in the $T \rightarrow 0$ limit)

$$\left[\Sigma_f^\sigma(\omega) \right]'' = \frac{\alpha}{2} \operatorname{sgn}(\omega) - \frac{1}{2\pi} |\omega - s_\sigma \mu_B B|. \quad (\text{B9})$$

Finally, the total self-energy in the $T \rightarrow 0$ limit is the sum of contributions from both spins

$$\begin{aligned} \Sigma_f''(\omega, B) &= \sum_{s_\sigma=\pm} \left[\Sigma_f^\sigma(\omega, B) \right]'' \\ &= \alpha \operatorname{sgn}(\omega) - \frac{1}{2\pi} (|\omega - \mu_B B| + |\omega + \mu_B B|). \end{aligned} \quad (\text{B10})$$

Above the unit of $\hbar = 1$ has been used; we will restore \hbar when necessary. Based on Eq. (B9), we conclude that the effect of Zeeman field on the self-energy $\Sigma_f^\sigma(\omega, B) = \Sigma_f^\sigma(\omega \rightarrow \omega - s_\sigma \mu_B B)$ is equivalent to a shift in fermionic frequency ω : $\omega \rightarrow \omega - s_\sigma \mu_B B$. This shift also applies to the self-energy $\Sigma_\xi^\sigma(\omega)$.

We now compute $\Sigma''_\xi(\omega)$ via [Eq. \(B1\)](#) at $T=0$. Following the analysis in Appendix E of Ref. [18], we have the following relation

$$\Sigma''_\xi(\omega, B=0) = -A + 2\Sigma''_f(\omega, B=0) \quad (\text{B11})$$

with A being an un-important constant. Based on the above result for $\Sigma''_f(\omega, B)$, we can generalize [Eq. \(B11\)](#) at a finite field $B \neq 0$ as

$$[\Sigma''_\xi(\omega, B)]'' = \frac{1}{2} \Sigma''_\xi(\omega \rightarrow \omega - s_\sigma \mu_B B, B). \quad (\text{B12})$$

The total self-energy $\Sigma''(\omega, B)$ reads

$$\begin{aligned} \Sigma''(\omega, B) &= \sum_{s_\sigma=\pm} [\Sigma''_\xi(\omega, B)]'' \\ &= -A + 2 \sum_{s_\sigma=\pm} [\Sigma''_f(\bar{\omega} = \omega - s_\sigma \mu_B B, B)]''. \end{aligned} \quad (\text{B13})$$

Plugging [Eq. \(B10\)](#) into [Eq. \(B13\)](#), since $[\Sigma''_f(\bar{\omega}, B)]'' = \alpha \operatorname{sgn}(\omega)/2 - |\bar{\omega} - s_\sigma \mu_B B|/2\pi$ ([Eq. \(B9\)](#)), we finally arrive (by restoring \hbar)

$$\begin{aligned} \Sigma''_\xi(\omega, B) &= -\frac{A}{\hbar} + 2 \sum_{s_\sigma=\pm} \left(\frac{\alpha}{2\hbar} \operatorname{sgn}(\omega) - \frac{1}{2\pi} \left| \omega - \frac{2s_\sigma \mu_B B}{\hbar} \right| \right) \\ &= -\frac{A}{\hbar} + \sum_{s_\sigma=\pm} \left(\frac{\alpha}{\hbar} \operatorname{sgn}(\omega) - \frac{2}{\pi} \left| \frac{\omega}{2} - \frac{s_\sigma \mu_B B}{\hbar} \right| \right). \end{aligned} \quad (\text{B14})$$

Note that in deriving [Eq. \(B14\)](#), the frequency ω in Σ''_ξ has been shifted twice by the Zeeman splitting: one in [Eq. \(B9\)](#) by f -fermions, and another in [Eq. \(B12\)](#) by ξ -fermions.

The physical gauge-invariant electron operator c_i is defined via ξ_{ij} -fermion as $c_i = \sum_j \xi_{ij} \phi_{ij} \sqrt{J}$ where ϕ_{ij} -fields represent fluctuating spinon pairing Δ_{ij} -fields and $G_\phi = 1/J$ [18]. It has been shown in Ref. [18] that $\Sigma''_c = \Sigma''_\xi/2$. As a result, at $T = 0$, we have

$$\frac{1}{\tau_B^c} = -2\Sigma''_c = -\Sigma''_\xi(\omega, B). \quad (\text{B15})$$

At finite temperatures and fields, we perform conformal transformation on Σ_c , similar to the case at zero-field [18, 21], leading to the scaling part of magneto-scattering rate:

$$\frac{\hbar/\tau_B^{s_\sigma}(\omega/T, B/T)}{\frac{2}{\pi} k_B T} = x^{s_\sigma} \coth \left(\zeta \frac{x^{s_\sigma}}{2} \right), \quad (\text{B16})$$

where $x^{s_\sigma} = (\hbar\omega/2 + s_\sigma \mu_B B)/k_B T$.

Note that in deriving [Eq. \(B16\)](#) from [Eq. \(B15\)](#) via conformal transformation, a tuning parameter ζ , allowed by conformal mapping of scattering rate in the scaling regime from zero temperature to finite temperatures [18, 21] (see Appendix E) is introduced to match the observed universal B/T -scaling in ω/T and B/T in magneto-scattering rate (see [Eq. \(1\)](#) and [Fig. 1](#) of maintext) whose value is constrained by the T -linear

Planckian coefficient α_T via via [Eq. \(B22\)](#), [Eq. \(C12\)](#), and [Eq. \(C26\)](#) [18].

After summing over the spin index $s_\sigma = \pm 1$ of [Eq. \(B16\)](#), the total magneto-scattering rate \hbar/τ_B (after subtracting the field independent T -linear residual scattering rate $\hbar/\tau_0(T) = (8/\pi)(1 - 1/\zeta)k_B T$) is given by

$$\begin{aligned} \frac{\hbar}{\tau_B} - \frac{\hbar}{\tau_0(T)} &= \\ &+ \frac{2}{\pi} k_B T \left(\left(\frac{\hbar\omega/2 + \mu_B B}{k_B T} \right) \coth \left(\zeta \frac{\hbar\omega/2 + \mu_B B}{2k_B T} \right) \right. \\ &\quad \left. + \left(\frac{\hbar\omega/2 - \mu_B B}{k_B T} \right) \coth \left(\zeta \frac{\hbar\omega/2 - \mu_B B}{2k_B T} \right) \right) \end{aligned} \quad (\text{B17})$$

We now discuss the scaling behaviors of [Eq. \(B17\)](#) in various limits.

(i) In the $B \rightarrow 0$ limit, [Eq. \(B17\)](#) reduces to

$$\frac{\hbar/\tau_B(B \rightarrow 0, \omega, T)}{k_B T} = \frac{\hbar/\tau_0(T)}{k_B T} + \frac{2}{\pi} \frac{\hbar\omega}{k_B T} \coth \frac{\zeta \hbar\omega}{4k_B T}. \quad (\text{B18})$$

This result may further reduce to the expressions in the following two limits:

(i)(a) The DC-limit ($B \rightarrow 0, \omega \rightarrow 0$) of T -linear Planckian scattering rate

$$\frac{\hbar}{\tau_B}(B \rightarrow 0, \omega \rightarrow 0, T) = \frac{\hbar}{\tau_0(T)} + \frac{8}{\pi \zeta} k_B T = \alpha_T k_B T \quad (\text{B19})$$

with $\alpha_T = 8/\pi$.

(i)(b) The AC-limit ($B \rightarrow 0, T \rightarrow 0$) of ω -linear scattering rate

$$\frac{\hbar}{\tau_B}(B \rightarrow 0, T \rightarrow 0, \omega) = \frac{2}{\pi} \hbar |\omega|. \quad (\text{B20})$$

(ii) In DC ($\omega \rightarrow 0$) limit, [Eq. \(B17\)](#) reduces to [Eq. \(3\)](#) of the main text

$$\frac{\hbar/\tau_B(\omega \rightarrow 0, B, T)}{k_B T} = \frac{\hbar/\tau_0(T)}{k_B T} + \frac{4}{\pi} \frac{\mu_B B}{k_B T} \coth \frac{\zeta \mu_B B}{2k_B T}. \quad (\text{B21})$$

This result may further reduce to the expressions in the following two limits:

(ii)(a) The zero-field, DC-limit ($\omega \rightarrow 0, B \rightarrow 0$) of T -linear Planckian scattering rate

$$\frac{\hbar}{\tau_B}(\omega \rightarrow 0, B \rightarrow 0, T) = \frac{\hbar}{\tau_0(T)} + \frac{8}{\pi \zeta} k_B T = \alpha_T k_B T. \quad (\text{B22})$$

(ii)(b) The $T \rightarrow 0$, DC-limit ($\omega \rightarrow 0, T \rightarrow 0$) of B -linear Planckian scattering rate

$$\frac{\hbar}{\tau_B}(\omega \rightarrow 0, T \rightarrow 0, B) = \alpha_B \mu_B B \quad (\text{B23})$$

with $\alpha_B = 4/\pi$.

In the exact $B = 0$ limit, the ω/T -scaling of the AC-scattering rate of LSCO at $p = 0.24$ has been observed in optical conductivity [3] and theoretically studied in Ref. [18], the result is

$$\frac{\hbar/\tau(B=0, \omega, T)}{k_B T} = \frac{2}{\pi} \frac{\hbar\omega}{k_B T} \coth \frac{\hbar\omega}{4k_B T}. \quad (\text{B24})$$

This result reduces to the following limiting cases:

(a) The DC-limit ($\omega \rightarrow 0$) of T -linear Planckian scattering rate

$$\frac{\hbar}{\tau}(B=0, \omega \rightarrow 0, T) = \alpha_T k_B T. \quad (\text{B25})$$

(b) The AC-limit ($B = 0, T \rightarrow 0, \omega$) of ω -linear scattering rate

$$\frac{\hbar}{\tau}(B=0, T \rightarrow 0, \omega) = \frac{2}{\pi} \hbar |\omega|. \quad (\text{B26})$$

It is clear that all the above results in various limits are consistent with each other.

Note that the value of the tuning parameter ζ only modify the transport properties at finite temperatures and finite fields, in particular the B/T -scaling behaviors in scattering rate and magneto-resistivity; however, it would not affect the transport coefficients both in the $T = 0$ limit (see Eq. (B23), and Eq. (B26)) and the exact zero-field ($B = 0$) limit (see Eq. (B24), and Eq. (B25)).

Appendix C: Universal scaling function $f(x)$

In this Appendix, we explain how we obtained the slope of the magneto-resistivity data as well as how we calculated the theoretical B/T -scaling of the slope.

1. Slope derivation for the experimental data of the magneto-resistivity in LSCO

Here we provide details concerning the data analysis performed to obtain the B/T -scaling of the slope of the magneto-resistance as shown in Fig. 2. Raw data for doping $p \in [0.161, 0.19]$ is taken from the available resources of [9].

Simply taking the discrete derivative of the raw data leads to very important fluctuations in the slope values. In order to avoid these large fluctuations, we decided to perform a slope window average analysis. The slope window average analysis consists in taking a regression line for points within an interval set by the window width w .

$$\frac{d\rho(B_i)}{dB_i} = \text{a of Fit}[a \cdot B + c = \rho(B) : B \in [B_i - w, B_i + w]]. \quad (\text{C1})$$

To illustrate this method, we plot in Fig. 6 the slope window of the magneto-resistivity using Eq. (C1) for $p = 0.19$ with $w = 5T$ (Fig. 6 (a)) and $w = 22T$ (Fig. 6 (b)). We

easily see that for smaller window widths some fluctuations persist, whereas for $w = 22T$ (Fig. 6 (b)) the slope values are very smooth. Additionally, taking a very large window width shifts the peak in the derivatives, sign of the transition towards superconductivity, towards higher values of magnetic fields and reduces the amplitude of the peak. Indeed, for windows widths which are very wide and include the transition to superconductivity, the values obtained from the linear regression, which is only valid in the strange metal phase (linear regime), will be affected by the inclusion of data which are in the superconducting state.

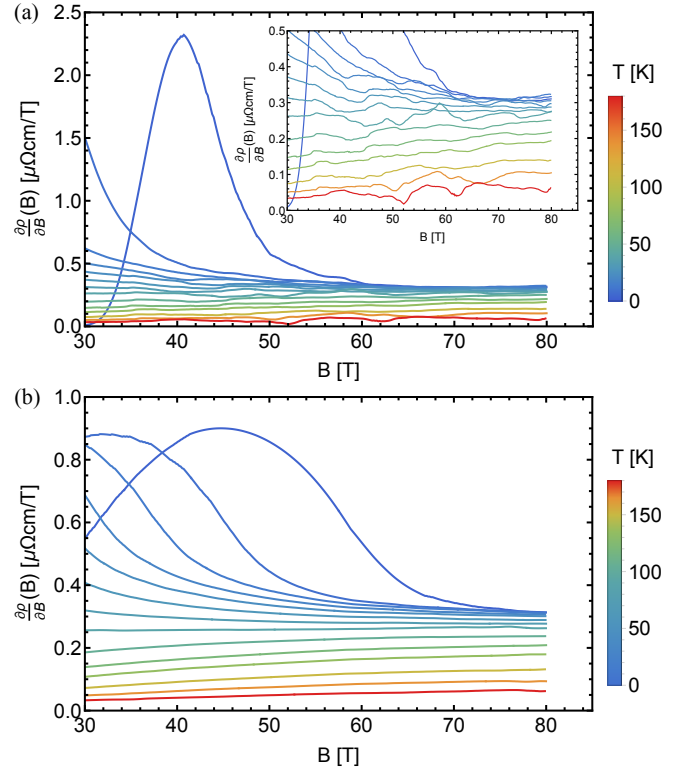


Figure 6. Slope window analysis of the magneto-resistivity data for $p = 0.19$ using Eq. (C1) with (a) $w = 5T$ and (b) $w = 22T$. While smaller window values still contain fluctuations, larger values exaggerate the superconductivity fluctuations at higher magnetic field values. The inset in (a) shows a zoom within the interval $[0, 0.5] \mu\Omega\text{cm}/\text{T}$ of the ordinate axis, where the slope fluctuations are visible

For Fig. 2 of the main text and Fig. 7, we choose to take the slope between values separated by a window width of $w = 5T$, which corresponds to an interval of about 57 data points. The slope of the magneto-resistivity is rescaled by a factor γ and plotted against the rescaled energy $\frac{\mu_B B}{k_B T}$, where $\gamma_{p=0.19} = 3.2(\mu\Omega\text{cm}/\text{T})^{-1}$ and $\beta_{p=0.19} = 3.06$ are fitting parameters. More precisely in Fig. 7 (a), we show the same data as in Fig. 6 (a), but rescaled as explained above. For clarity, we only plot the higher magnetic field data points where the curves have a linear slope or start to become superconducting, but we discard the parts in the superconducting phase

as shown in Fig. 7 (b) for $p = 0.19$. Fig. 2 (b) is reproduced from the same data as Fig. 7 (b).

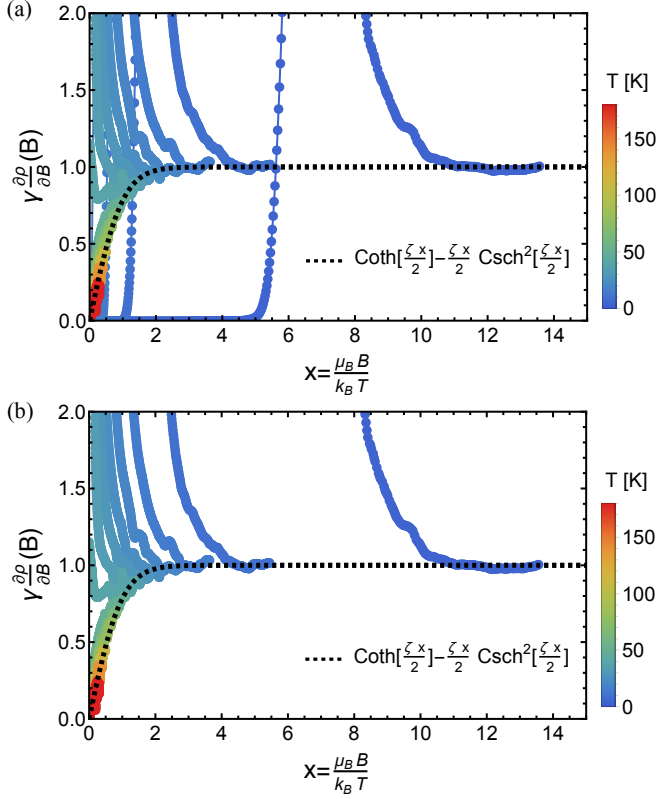


Figure 7. B/T -scaling of the rescaled slope of the magneto-resistivity for $p = 0.19$ where in the panel (a) is shown the slope of the magneto-resistivity with a window averaging of $w = 5$ T [Eq. (C1)] with identical parameter as in Fig. 1 and Fig. 2: $\gamma = 3.2(\mu\Omega\text{cm})^{-1}\text{T}$, and $\zeta = 3.06$. The red dotted line corresponds to the theoretical prediction of the derivative of the magneto-resistivity given in Eq. (C19) with $\zeta = 3.06$. In (b) is represented the same data as in (a) but points at lower magnetic field values in the superconducting phase have been truncated.

For $p = 0.184$, $p = 0.170$, and $p = 0.161$, we follow a similar procedure, and we obtain the slope by window averaging with $w = 1.5$ T (which corresponds to about 55 data points) for the three doping values as shown in Fig. 8.

Unfortunately, the magneto-resistivity data for doping $p \in [0.161, \dots, 0.184]$ were only taken up to 55 T, and for a temperature interval of $T \in [10, \dots, 60]$. This makes the scaling of the experimental data harder to see. Indeed as shown in Fig. 8, the data just saturate on the scaling function (red curve). Lower temperature and higher magnetic field data would allow to recover the plateau as it is the case for $p = 0.19$ (see Fig. 7 (b) or Fig. 2 (b)).

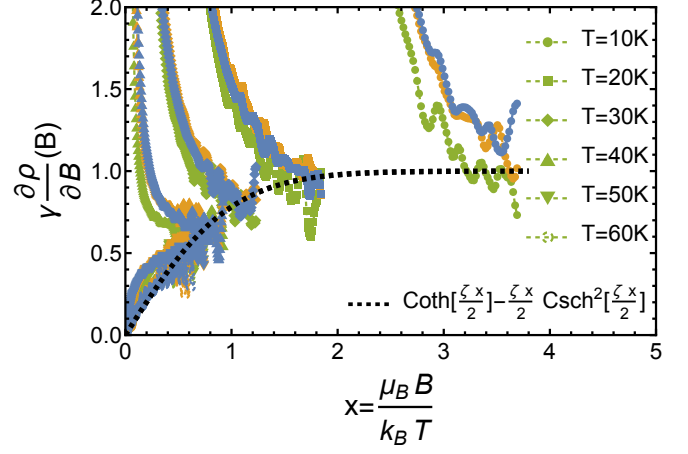


Figure 8. B/T -scaling of the rescaled slope of the magneto-resistivity in function of $x = \mu_B B / (k_B T)$ for doping $p = 0.161, 0.170$, and 0.184 , using the window averaging procedure with $w = 1.5$ T [Eq. (C1)] for parameters given by $\gamma_{p=0.161} = 1.3(\mu\Omega\text{cm})^{-1}\text{T}$, $\gamma_{p=0.170} = 1.6(\mu\Omega\text{cm})^{-1}\text{T}$, $\gamma_{p=0.184} = 1.9(\mu\Omega\text{cm})^{-1}\text{T}$, and $\zeta = 3.06$ for all three doping values. Note that γ depends on the carrier density $n = 1/V$ as well as the effective mass [Eq. (C20)] and is expected to vary for different doping values. The red dotted line corresponds to the theoretical prediction of the derivative of the magneto-resistivity given in Eq. (C19) with $\zeta = 3.06$.

In Fig. 9, we show the values of the slope obtained by window average for $p = 0.19$ at different magnetic field rescaled by γ in function of T/B . In Fig. 9 (a) we compare the rescaled magneto-resistivity slope values with our theoretical prediction [Eq. (C19)], where the black line corresponds to $(\coth(\zeta x/2) - \zeta x/2 \operatorname{csch}^2(\zeta x/2))$ with $x = \mu_B B / (k_B T)$, $\gamma_{p=0.19} = 3.2(\mu\Omega\text{cm}/\text{T})^{-1}$, and $\zeta = 3.06$. In Fig. 9 (b), we show the same data set for the rescaled magneto-resistivity slope values as in (a), but we compare the data to the marginal Fermi-liquid (MFL) empirical quadratic scaling approximation [10, 11]:

$$\rho^{MFL}(B, T) = \rho_0^{MFL}(T) + \sqrt{(a_1 T)^2 + (B/\gamma)^2}. \quad (C2)$$

Taking the derivative with respect to magnetic field leads to

$$\frac{d\rho^{MFL}}{dB} = \frac{1}{\gamma} \frac{1}{\sqrt{(a_1 \gamma T/B)^2 + 1}}, \quad (C3)$$

where we set $\gamma = 3.2(\mu\Omega\text{cm}/\text{T})^{-1}$ (same value as for the scaling function) and where we find $a_1 = 0.407\mu\Omega\text{cm}/\text{K}$ as the optimum parameter value. The dashed black line in Fig. 9 (b) corresponds to $\gamma d\rho^{MFL}/dB = \sqrt{(a_1 \gamma T/B)^2 + 1}^{-1}$.

The insets in Fig. 9 (a) and (b) show a zoom where the data form a plateau at small T/B values. We note that the scaling function arising from our prediction allows to account well for this feature (inset of Fig. 9 (a)), whereas the MFL approximation shows a constant increase when approaching zero (inset of Fig. 9 (b)).

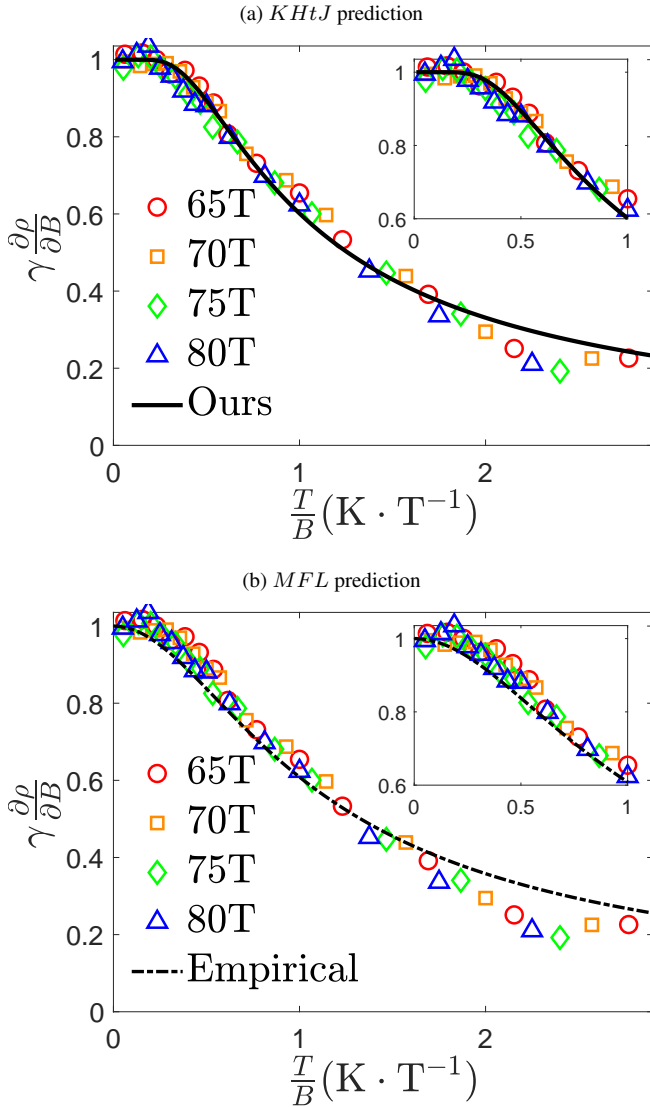


Figure 9. (a) Rescaled magneto-resistivity slope values compared to our theoretical prediction [Eq. (C19)], where the black line corresponds to $(\coth(\zeta x/2) - \zeta x/2 \operatorname{csch}^2(\zeta x/2))$ with $x = \mu_B B/(k_B T)$, $\gamma_{p=0.19} = 3.2(\mu\Omega\text{cm}/\text{T})^{-1}$, and $\zeta = 3.06$. (b) Same data set of the rescaled magneto-resistivity slope values as in (a), but compared to the marginal Fermi-liquid (MFL) approximation [10, 11] [Eq. (C2)], where the dashed black line corresponds to $\gamma d\rho^{MFL}/dB = \sqrt{(a_1 \gamma T/B)^2 + 1}^{-1}$ with $\gamma = 3.2(\mu\Omega\text{cm}/\text{T})^{-1}$ and $a_1 = 0.407 \mu\Omega\text{cm}/\text{K}$. We note that the scaling function arising from our prediction allows to account for the small plateau observed at small T/B values, while the MFL approximation shows a constant increase when approaching zero, as shown in the insets of (a) and (b).

For completeness, in Fig. 10, we show magneto-resistivity for $p = 0.20$, where the raw data is taken from [39]. We follow a similar approach to what we performed for $p = 0.19$ in Fig. 1 (b). We note that for $p = 0.20$ magneto-resistivity data in the B -linear limits are well-fitted by Eq. (1), with parameter given by $c_0 = 8.82 \mu\Omega\text{cm}$, $c_1 = 0.86 \mu\Omega\text{cmK}^{-1}$, $\gamma = 3.2(\mu\Omega\text{cm})^{-1}\text{T}$, $\zeta = 6.27$. We note that some of these

parameters are different from the $p = 0.19$ case, which is not surprising since these two experiments were done independently and with different samples. Deviations at low magnetic field values between theoretical predictions (dashed lines) and the data at low temperatures are interpreted as coming from the crossover into the superconducting state. Indeed, the deviation vanishes at higher magnetic field values and at a higher temperature well above T_c where superconductivity is absent.

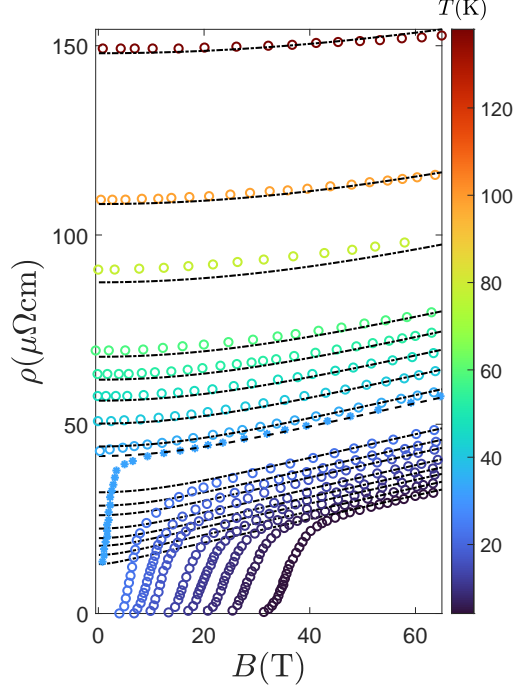


Figure 10. Magneto-resistivity data for $p = 0.20$ versus magnetic field at different temperatures reproduced from [39]. Colored symbols represent experimental data and black dotted lines correspond to the theoretical prediction given in Eq. (1) with parameter given by $c_0 = 8.82 \mu\Omega\text{cm}$, $c_1 = 0.86 \mu\Omega\text{cmK}^{-1}$, $\gamma = 3.2(\mu\Omega\text{cm})^{-1}\text{T}$, $\zeta = 6.27$.

2. Analytical B/T-scaling of the slope of the magneto-resistivity

Here we provide the theoretical calculation of the slope of the magneto-resistivity. We start by considering the results that we obtained for the scattering rate within the strange metal phase in the DC limit ($\omega \rightarrow 0$) [Eq. (3)]

$$\frac{\hbar}{\tau(B, T)} - \frac{\hbar}{\tau_0(T)} = \frac{4}{\pi} k_B T \frac{\mu_B B}{k_B T} \coth\left(\zeta \frac{\mu_B B}{2k_B T}\right) \quad (\text{C4})$$

In the zero temperature limit this leads to

$$\lim_{T \rightarrow 0} \left[\frac{\hbar}{\tau(B, T)} - \frac{\hbar}{\tau_0(T)} \right] = \frac{4}{\pi} k_B T \frac{\mu_B B}{k_B T} \quad (\text{C5})$$

$$= \frac{4}{\pi} \mu_B B \quad (\text{C6})$$

$$\equiv \alpha_B \mu_B B \quad (\text{C7})$$

where the linear-in-field Planckian coefficient is given by

$$\alpha_B = \frac{4}{\pi} \quad (C8)$$

Similarly, In the zero field limit this leads to

$$\lim_{B \rightarrow 0} \left[\frac{\hbar}{\tau(B, T)} - \frac{\hbar}{\tau_0(T)} \right] = \frac{8}{\pi} \frac{1}{\zeta} k_B T \quad (C9)$$

$$(C10)$$

Here, the purely temperature-dependent T-linear scattering rate $\hbar/\tau_0(T)$ corresponds to the purely temperature-dependent T-linear resistivity $\rho_0(T)$ observed in experiment (see Eq. (1) of main text) with $\rho_0(T) = m^*/(ne^2)1/\tau_0$.

We therefore consider the temperature only contribution scattering rate $\hbar/\tau_0(T)$ to also be purely temperature-dependent with a T-linear dependence:

$$\frac{\hbar}{\tau_0(T)} = b k_B T \quad (C11)$$

with $b = 8(1 - 1/\zeta)/\pi$ in order to retrieve the the linear-in-temperature Planckian coefficient as follows:

$$\lim_{B \rightarrow 0} \left[\frac{\hbar}{\tau(B, T)} \right] = (1 - \frac{1}{\zeta}) \frac{8}{\pi} k_B T + \frac{8}{\pi} \frac{1}{\zeta} k_B T \quad (C12)$$

$$= \frac{8}{\pi} k_B T \quad (C13)$$

$$\equiv \alpha_T k_B T \quad (C14)$$

with

$$\alpha_T = \frac{8}{\pi} = 2\alpha_B \quad (C15)$$

Using the DC Drude formula for resistivity, we have

$$\begin{aligned} (\rho(B, T) - \rho_0(T)) &= \frac{m^*}{\hbar n e^2} \left(\frac{\hbar}{\tau(B, T)} - \frac{\hbar}{\tau_0(T)} \right) \\ &= \frac{m^*}{\hbar n e^2} \alpha_B k_B T \frac{\mu_B B}{k_B T} \coth\left(\frac{\zeta \mu_B B}{2k_B T}\right) \end{aligned} \quad (C16)$$

where we used Eq. (C8). Defining,

$$\rho_1(B, T) \equiv \rho(B, T) - \rho_0(T) \quad (C17)$$

$$\begin{aligned} \frac{\partial \rho_1(B, T)}{\partial B} &= \frac{\mu_B}{k_B T} \frac{\partial (\rho_1(B, T))}{\partial \frac{\mu_B B}{k_B T}} \\ &= \frac{\mu_B m^*}{\hbar n e^2} \alpha_B \frac{\partial}{\partial \frac{\mu_B B}{k_B T}} \left[\frac{\mu_B B}{k_B T} \coth\left(\frac{\zeta \mu_B B}{2k_B T}\right) \right] \\ &= \frac{\mu_B m^*}{\hbar n e^2} \alpha_B \frac{\partial}{\partial x} \left[x \coth\left(\frac{\zeta x}{2}\right) \right] \\ &= \frac{\mu_B m^*}{\hbar n e^2} \alpha_B \left[\coth\left(\frac{\zeta x}{2}\right) - \frac{\zeta x}{2} \operatorname{csch}^2\left(\frac{\zeta x}{2}\right) \right] \end{aligned} \quad (C18)$$

with $x = \frac{\mu_B B}{k_B T}$,

$$\begin{aligned} \gamma \frac{\partial \rho_1(B, T)}{\partial B} &= f(x), \\ f(x) &= \coth\left(\frac{x}{2}\right) - \zeta \frac{x}{2} \operatorname{csch}^2\left(\frac{x}{2}\right) \end{aligned} \quad (C19)$$

where we defined

$$\gamma \equiv \frac{\hbar n e^2}{\mu_B m^* \alpha_B}. \quad (C20)$$

We rewrite the empirical formula for resistivity (Eq. (1)) as

$$\rho(B, T) = c_0 + c_1 T + \frac{B}{\gamma} \coth \frac{\zeta \mu_B B}{2k_B T}, \quad (C21)$$

which in the zero field ($B \rightarrow 0$) limit becomes

$$\rho(B \rightarrow 0, T) = c_0 + \left[c_1 + \frac{2k_B}{\gamma \zeta \mu_B} \right] T. \quad (C22)$$

On the other hand, the AC resistivity is given by [18, 21]

$$\rho(\omega, T) = c_0 + \frac{m^*}{ne^2 \hbar} \frac{2\hbar\omega}{\pi} \coth \frac{\hbar\omega}{2k_B T}, \quad (C23)$$

which in the static ($\omega \rightarrow 0$) limit takes

$$\rho(\omega \rightarrow 0, T) = c_0 + \frac{m^*}{ne^2 \hbar} \alpha_T k_B T. \quad (C24)$$

Comparing Eq. (C22) with Eq. (C24) results in

$$c_1 = \frac{m^* k_B}{ne^2 \hbar} \left[\alpha_T - \frac{2\alpha_B}{\zeta} \right], \quad (C25)$$

where we have used Eq. (C20). For $\alpha_T = 2\alpha_B$ (Eqs. (C8) and (C15)), we obtain

$$c_1 = \frac{m^* k_B}{ne^2 \hbar} \left[1 - \frac{1}{\zeta} \right] \alpha_T, \quad (C26)$$

which can be rewritten in terms of γ and ζ as

$$c_1 = \frac{2k_B}{\gamma \mu_B} \left[1 - \frac{1}{\zeta} \right]. \quad (C27)$$

Table (II) below shows the estimated values of γ (using Eq. (C20)) and c_1 (taking Eq. (C27)) compared to the fitting ones (in parentheses).

p	m^*/m_e	γ (T/ $\mu\Omega\cdot\text{cm}$)	c_1 ($\mu\Omega\cdot\text{cm}/\text{K}$)
0.19	14.86 (13.81)	3.7 (3.2)	0.513 (0.598) [0.654]
0.20	13.75 (12.47)	4.0 (3.5)	0.475 (0.547)

Table II. The estimated (fitted) [optimized] parameters used for the doping range $0.19 \leq p \leq 0.2$. Note that the estimated values of the effective mass are taken from Ref. [8].

We actually use 3 different ways to estimate the various parameter values:

1) we use an estimate of m^* from Ramshaw, use $n = 1/V$, and we use $\alpha_T = 8/\pi$ and $\alpha_B = 4/\pi$, as well as the fitted value for $\zeta = 3.06$. With this we can make the analytical estimated values for γ and c_1 . This corresponds to the values not in parentheses nor brackets.

2) we use the fitted value of γ such that $\gamma \frac{\partial \rho}{\partial B} (\mu B \gg k_B T) \rightarrow 1$ as well as $n = 1/V$ and $\alpha_B = 4/\pi$ to get a "fitted" estimate of m^* , we then use this fitted value of m^* to further estimate the "fitted" value of c_1 , with $\alpha_T = 8/\pi$ and $\zeta = 3.06$. This corresponds to the values in parentheses.

3) for $p = 0.19$, we have an optimized value of c_1 , such that the fit $\rho(B, T) = c_0 + c_1 T + \frac{B}{\gamma} \coth(\zeta \frac{\mu_B B}{2k_B T})$ follows nicely ρ vs T for different B as plotted in Fig. 1 (a), where we use the fitted value of γ (see point 2 above) which gave us $c_1 = 0.654$. This corresponds to the value in brackets.

Appendix D: Planckian coefficients

Here we describe how we obtained the Planckian coefficients α_T and α_B from the experimental magneto-resistivity data from [9]. These coefficients are the proportionality factors between the scattering rate and the energy scales $k_B T$ in the DC and zero-field limit or $\mu_B B$ in the DC limit and zero temperature limit respectively

$$\lim_{B \rightarrow 0} \left[\frac{\hbar}{\tau(B, T)} \right] = \alpha_T k_B T, \quad (\text{D1a})$$

$$\lim_{T \rightarrow 0} \left[\frac{\hbar}{\tau(B, T)} \right] = \alpha_B \mu_B B, \quad (\text{D1b})$$

where our theoretical predictions yield $\alpha_T = \frac{8}{\pi}$ and $\alpha_B = \frac{4}{\pi}$.

In order to estimate experimentally the Planckian coefficients α_T and α_B , we start from the DC Drude formula for the resistivity

$$\rho(B, T) = \frac{m^*}{\hbar n e^2} \frac{\hbar}{\tau(B, T)}. \quad (\text{D2})$$

Combining with Eq. (D1), we can relate the slope of resistivity with respect to either temperature A_T^1 or with respect to magnetic field A_B^1

$$\lim_{B \rightarrow 0} [\rho(B, T)] = \frac{m^*}{\hbar n e^2} \alpha_T k_B T \equiv A_T^1 T, \quad (\text{D3a})$$

$$\lim_{T \rightarrow 0} [\rho(B, T)] = \frac{m^*}{\hbar n e^2} \alpha_B \mu_B B \equiv A_B^1 B, \quad (\text{D3b})$$

where we identify

$$A_T^1 = \frac{m^*}{\hbar n e^2} \alpha_T k_B, \quad (\text{D4a})$$

$$A_B^1 = \frac{m^*}{\hbar n e^2} \alpha_B \mu_B. \quad (\text{D4b})$$

Inverting these relations allows us to determinate the Planckian coefficients α_T and α_B from the values of the slope the

resistivity

$$\alpha_T = \frac{\hbar n e^2}{m^*} k_B^{-1} A_T^1, \quad (\text{D5a})$$

$$\alpha_B = \frac{\hbar n e^2}{m^*} \mu_B^{-1} A_B^1. \quad (\text{D5b})$$

From Eq. (D5), we see that in order to determinate the values of the Planckian coefficients α_T and α_B , we also need to estimate the ratio of effective electron mass m^* to the carrier density n , n/m^* . There are two ways to estimate this ratio: one by plasma frequency ω_p , the other by separating estimating m^* via specific heat coefficient and n via other transport measurements, as described below.

a. Estimation of n/m^* from plasma frequency measurements

To estimate n/m^* shown in Eq. (D5), we follow the measurements of the plasma frequency ω_p^2 [8], where the plasma frequency is given by

$$\omega_p^2 = 4\pi e^2 \frac{n}{m^*}. \quad (\text{D6})$$

The n/m^* derived from experimental data of the plasma frequency at low doping $p < 0.2$ is well approximated by a linear regression given by [8]

$$\frac{n}{m^*} = \frac{0.42p}{la^2 m_e}, \quad (\text{D7})$$

where p is the doping percentage, $a \simeq 0.378$ nm is in the in-plane lattice spacing, and $l \simeq 0.66$ nm corresponds to the half-interlayer spacing, and m_e to the bare electron mass. See [8] and Fig. 4B therein.

Replacing Eq. (D7) in Eq. (D5), we get

$$\alpha_T = \frac{A_T^1 \hbar e^2}{k_B} \frac{0.42p}{la^2 m_e}, \quad (\text{D8a})$$

$$\alpha_B = \frac{A_B^1 \hbar e^2}{\mu_B} \frac{0.42p}{la^2 m_e}. \quad (\text{D8b})$$

Similarly to the results using effective mass estimations from specific heat measurements, the parameters A_T^1 and A_B^1 correspond to the slope of the resistivity curves obtained from [9] for LSCO, as details above in Appendix D 1 and D 2. The values of the Planckian coefficients obtained from plasma frequency measurements through Eq. (D8) are shown in Fig. 3.

b. Estimation of n/m^* by separately estimating m^* and n

The n/m^* ratio can also be estimated by separately estimating m^* and n . Following Ref. [8], the electron effective mass m^* is taken to be inversely proportional to doping p by specific heat measurements, $m^* \propto 1/p$. More precisely, we use the fact $m^* \propto p^{-1}$ in the overdoped regime, where effects from the pseudogap phase are absent, and extrapolate to lower doping values [8, 40]. To estimate the carrier density n ,

we follow the argument in [8] by plasma frequency measurement, where the square of plasma frequency ω_p^2 obtained from optical conductivity measurements grows linearly with doping for doping withing the interval of interest $p \in [0, 0.3]$ and that for an parabolic band it is proportional to n/m^* , $\omega_p^2 \propto n/m^*$. Since $\omega_p^2 \propto n/m^* \propto p$ and $m^* \propto p^{-1}$ according to specific heat measurement, we conclude that in our doping range of interest $p \in [0.161, 0.19]$, the carrier density is close to an effective constant value [8]

$$n \approx n_{eff} \approx \frac{1}{a^2 l}, \quad (D9)$$

where $a \simeq 0.378$ nm is in the in-plane lattice spacing, and $l \simeq 0.66$ nm such that $c = 2l$ corresponds to the interlayer spacing. We use l instead of c , because there are 2 superconducting copper oxide planes separated by l within a single unit cell [8].

On the other hand, the Fermi surface reconstruction of cuprates was observed from Hall measurement [10], where the carrier density is proportional to doping at low doping values $n[p < 0.15] \propto p$ and goes as $1 + p$ for large doping values when the system reaches the Fermi liquid phase phase on the overdoped side $n[p > 0.3] \propto 1 + p$. It seems that in between these two regions, the carrier density still grows linearly with doping $n[p < 0.15] \propto p$ with the overdoped $n[p > 0.3] \propto 1 + p$ regimes. To reconcile the discrepancy between the doping insensitive $n_{eff} \sim 1/V$ estimated here and the doping dependent carrier density n via the Hall coefficient measurement goes beyond the scope of the present work and deserves further study elsewhere.

As illustrated in Fig. 11, we choose a wide band of plausible estimate of the effective mass, given by the area between the green (m_{max}^*) and red (m_{min}^*), such that the estimate (m_{av}^*) depicted as the orange curve is given by the average of (m_{max}^*) and (m_{min}^*). For simplicity, we parametrize these in function of doping p as

$$m_{min}^*/m_e = 1.5/p, \quad (D10a)$$

$$m_{av}^*/m_e = 2.5/p, \quad (D10b)$$

$$m_{max}^*/m_e = 3.5/p. \quad (D10c)$$

These values are used to determine the Planckian coefficients shown in Fig. 20. In Fig. 20, we compare the Planckian coefficients estimated by the two approaches mentioned above, they show excellent agreement.

In the next two sections we explain in details how we calculate the slope of experimentally measured resistivity with respect to either temperature A_T^1 or with respect to magnetic field A_B^1 . Once these values are known, we use Eq. (D5), with Eq. (D10b) and Eq. (D9), to evaluate the Planckian coefficients α_T and α_B , which corresponds to the blue circles and purple squares in Fig. 3 respectively. The error bars on the Planckian coefficients α_T and α_B are given by the upper m_{max}^* and lower m_{min}^* bound estimates. From Eq. (D5), it is clear the upper bound m_{max}^* will give the lower bound estimates of the Planckian coefficients, and lower m_{min}^* bound will give the upper estimation.

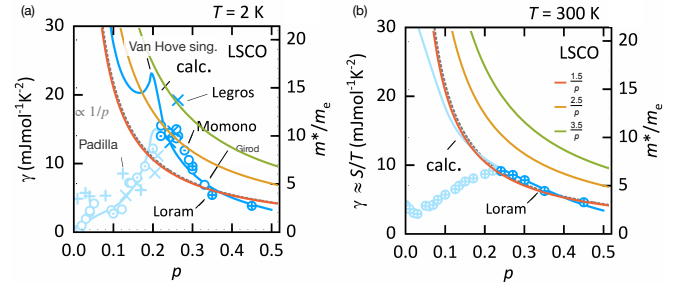


Figure 11. Estimation of m^*/m_e from specific heat measurements [8]. A plausible estimate of the effective mass is illustrated by the middle orange curve ($m_{av}^*/m_e = 2.5/p$). Additionally, upper bound and lower bound estimates are parametrized by ($m_{max}^*/m_e = 3.5/p$) and ($m_{min}^*/m_e = 1.5/p$) respectively. These values are used to determine the Planckian coefficients in Fig. 3 of the main text. Figures are reproduced from [8]

1. Linear-in-temperature Planckian coefficients

In this section, we explain how we obtained the linear-in-temperature Planckian coefficients α_T from the experimental data in [9]. As explain above, one need to determine the slope of resistivity with respect to temperature A_T^1 . For this we use the zero-field data and parametrize the resistivity as

$$\rho(T) = \rho_0 + A_T^1 T \quad (D11)$$

and proceed to a linear fit of the experimental data in order to extract A_T^1 . As an illustration in Fig. 12 for $p = 0.161$ in (a) and $p = 0.190$ in (b), we show the experimental data of the resistivity with respect to temperature at zero magnetic field in blue, the data used to perform the linear fitting in orange and the obtained numerical linear regression as the black dashed line. The value obtained of the parameters A_T^1 and ρ_0 from the linear fit [Eq. (D11)] for all doping values are shown in Fig. 13. We note that A_T^1 shows a monotonic, almost linear decrease with doping, consistent with the fact that $1/A_T^1$ exhibits a linear dependence with respect to doping (see [8] and Fig. 1B therein). Whereas ρ_0 does not show any regular pattern and is relatively small compare to the values of the resistivity in the temperature range of interest.

Finally, using Eq. (D5)–Eq. (D10), the slope values A_T^1 are used to estimate the linear-in-temperature α_T Planckian coefficients shown in Fig. 3.

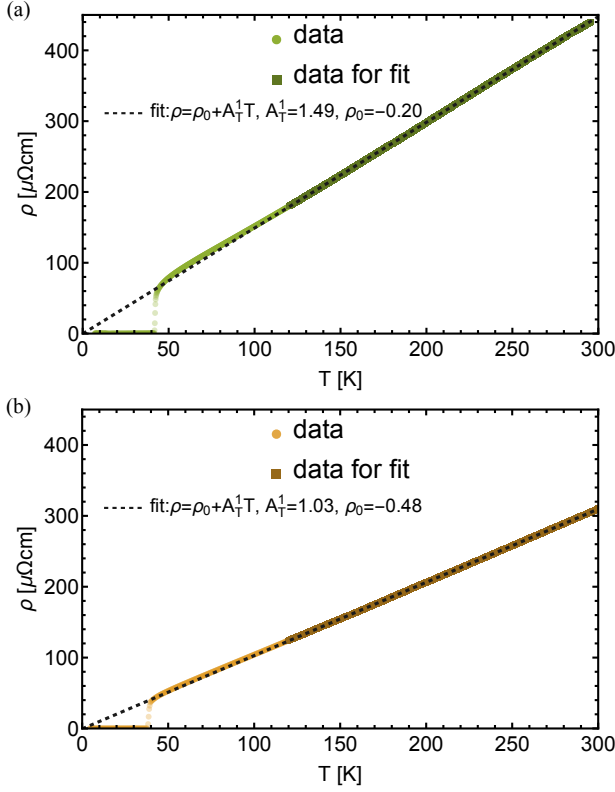


Figure 12. Resistivity data with respect to temperature at zero magnetic field reproduced from [9] for (a) $p = 0.161$, and (b) $p = 0.190$. Colored lines correspond to the experimental data, darker parts of the data are used to perform the linear regression, and the black dashed line correspond to the obtained linear fit from which we extract the slope value A_T^1 used to estimate the linear-in-temperature Planckian coefficients shown in Fig. 3. The value obtained of the parameters A_T^1 and ρ_0 from the linear fit [Eq. (D11)] for all doping values are shown in Fig. 13

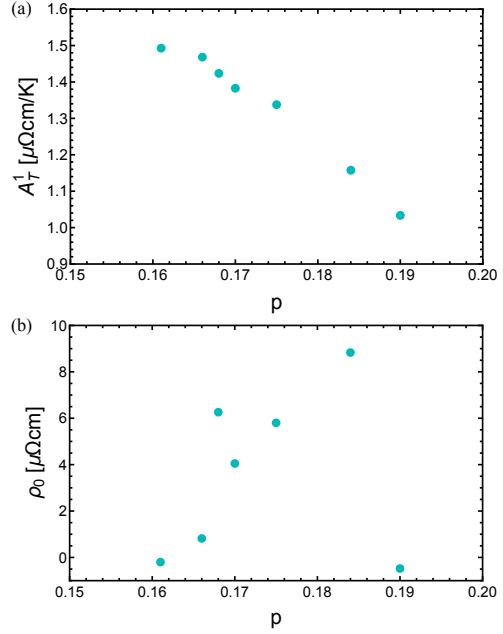


Figure 13. Parameters values for (a) the slope A_T^1 and (b) the residual zero-field resistivity ρ_0 obtained from the linear fit [Eq. (D11)] plotted versus doping values. A_T^1 shows a monotonic, almost linear decrease with doping, while ρ_0 does not show any specific doping dependence. The slope values A_T^1 are further used through Eq. (D5)–Eq. (D10) to estimate the linear-in-temperature Planckian coefficients shown in Fig. 3

2. Linear-in-field Planckian coefficients

Here we explain how we obtained the linear-in-field Planckian coefficients α_B from the experimental data in [9]. As explained above, one needs to determine the slope of resistivity with respect to magnetic field A_B^1 . We follow a similar procedure to the determination of the in-temperature linear coefficient A_T^1 described above, to the difference that for a given doping we will obtain various values A_B^1 depending on temperature. Indeed, as shown in Fig. 14 (a) for $p = 0.161$ and (b) for $p = 0.190$, magneto-resistivity curves were taken at various temperatures. In order to determine A_B^1 from the experimental data, we parametrize the resistivity as

$$\rho(B) = \rho_0 + A_B^1 B \quad (\text{D12})$$

and proceed to a linear fit of the experimental data at the available temperatures and for all doping. For simplicity, we here use a linear regression to determine the slope A_B^1 instead of performing the window slope analysis described in Appendix C. In Fig. 18, we later show that the two methods are almost equivalent.

In Fig. 14 (a) for $p = 0.161$ and (b) for $p = 0.190$, we show the experimental data of the resistivity with respect to magnetic field at various temperatures in the temperature scaled color scheme. The data used to perform the linear fitting are shown in orange and the obtained numerical linear regressions

are represented by the black dashed lines. The value obtained for the parameters A_B^1 and ρ_0 from the linear fit [Eq. (D12)] are shown in Fig. 15 (a) and (b) respectively, plotted versus doping for the different temperatures ; and they are shown plotted versus temperature for the different doping values in Fig. 16 (a) and (b) respectively.

We note that A_B^1 versus doping shows a similar monotonic, almost linear decrease with doping for all temperature values as shown in Fig. 15 (a), which is consistent with the behavior of the linear-in-temperature coefficient A_T^1 [Fig. 13 (a)]. In Fig. 15 (b), we see that ρ_0 versus doping does not show any specific doping dependence.

However, when plotted against temperature we note that ρ_0 shows a linear temperature dependence for all doping as illustrated in Fig. 16 (b). This implies that the zero-field resistivity contains a linear-in-temperature dependence. For this reason, we introduce an extra explicit temperature only dependence of the resistivity given by $\rho_0(T) = c_0 + c_1 T$ in Eq. (1), which through the DC formula [Eq. (D2)] leads to an extra explicit temperature only dependence of the scattering rate expressed as $\hbar/\tau_0(T)$.

This extra explicit temperature only dependence of the resistivity given by $\rho_0(T) = c_0 + c_1 T$ in Eq. (1) turns out to be of crucial importance when explaining the experimental data. Indeed as shown in Fig. 17 and Fig. 1 (a) in the main text, it allows to account for the slight change of the slope of the resistivity with respect to temperature. In Fig. 17 we clearly show the contribution of each of the terms in the expression for the resistivity in Eq. (1). The added temperature only dependence $\rho_0(T) = c_0 + c_1 T$ is represented by the pink line, the theoretical scaling function $\rho_1(B, T) = \frac{B}{\gamma} \coth \frac{\zeta \mu_B B}{2k_B T}$ by the blue line, which saturates at low temperatures, and the total contribution by the black lines. This results in a slight change of slope of the resistivity enhanced by the black dashed lines in Fig. 17 around $T_{kink} \sim 60$ K. This feature is likewise observed in the experimental data, and the theoretical predictions are in excellent agreement with the measurements.

In Fig. 16 (a), we see that A_B^1 versus temperature shows a monotonic decrease for all doping values. For $p = 0.19$, we observe a saturation plateau at low temperature. For other doping values, magneto-resistivity data were only taken down to 10 K, which is unfortunately too high to see the appearance of the saturation plateau. We also note that these features are well described by our theoretical scaling function as shown in Fig. 9 and Fig. 2 (a) for different magnetic field values for $p = 0.19$.

In Fig. 18, we show the slope of the resistivity data versus temperature for $p = 0.19$ using the values obtained by linear regression A_B^1 (purple circles) and the values obtained from the window slope analysis $d_B \rho(B = 80T)$ method described in Appendix C at high magnetic field (80 T) with a window width of $w = 22$ T, that is the saturation values of the slope in Fig. 6 (b) at $B = 80$ T. We see that the two methods are in good agreement.

Because for lower doping values, the zero temperature limit of A_B^1 is not available experimentally, and in order to avoid effects arising from the neighboring superconducting fluctuations at low temperature, we choose to estimate the slope of

resistivity at finite temperature by taking the average between $T \in [20, 30]$ K. Indeed, we observed that for instance in the $p = 0.161$ case in Fig. 14 (a), the resistivity data at $T = 10$ K are just barely linear with magnetic field at the highest measured magnetic field values (55 T), and are clearly affected by superconducting fluctuations below $B = 45$ T. We therefore believe that our estimation at low temperature is not optimal and measurements at higher magnetic field values would be necessary for a more accurate estimation, as was performed for $p = 0.19$. Therefore, we choose to take average between $T \in [20, 30]$ K, this means

$$A_B^1 = \frac{A_B^1(T = 20\text{K}) + A_B^1(T = 25\text{K}) + A_B^1(T = 30\text{K})}{3}, p = 0.19 \quad (\text{D13})$$

$$A_B^1 = \frac{A_B^1(T = 20\text{K}) + A_B^1(T = 30\text{K})}{2}, p \in [0.161, \dots, 0.184] \quad (\text{D14})$$

The slope values obtained from the linear regression A_B^1 divided by μ_B are shown in Fig. 19 (a), alongside the previously obtained linear-in-temperature coefficient A_T^1 divided by k_B (see Appendix D 1). We note that both the in-temperature A_T^1/k_B and in-field A_B^1/μ_B rescaled coefficients follow a similar trend with respect to doping, such that their ratio $A_T^1 \mu_B / (A_B^1 k_B)$ illustrated in Fig. 19 (b) is almost doping independent, and close to 2 for all doping values. From Eq. (D4), it is easy to see that this ratio corresponds to the ratio of the Planckian coefficients α_T/α_B , for which our theoretical prediction yields exactly 2, since our theoretical scaling predicts $\alpha_T = \frac{8}{\pi}$ and $\alpha_B = \frac{4}{\pi}$ (see Appendices B and C 2).

Finally, using Eq. (D5)–Eq. (D10), the slope values A_T^1 and A_B^1 are used to estimate the linear-in-temperature α_T and linear-in-field α_B Planckian coefficients shown in Fig. 20.

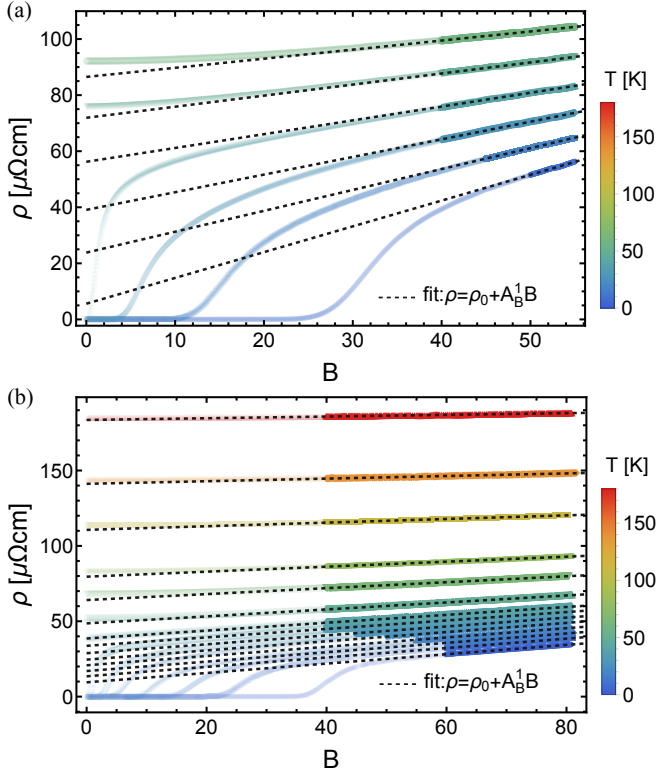


Figure 14. Resistivity data with respect to magnetic field at various temperature values reproduced from [9] for (a) $p = 0.161$, and (b) $p = 0.190$. Colored lines correspond to the experimental data and are associated to the temperature color scheme, the darker parts of the data are used to perform the linear regression, and the black dashed lines are the obtained linear fits from which we extract the slope value A_B^1 used to calculate the Planckian coefficients. The obtained fitting parameters Fig. 15 (a) and (b) respectively, plotted versus doping for the different temperatures ; and they are shown plotted versus temperature for the different doping values in Fig. 16 (a) and (b) respectively.

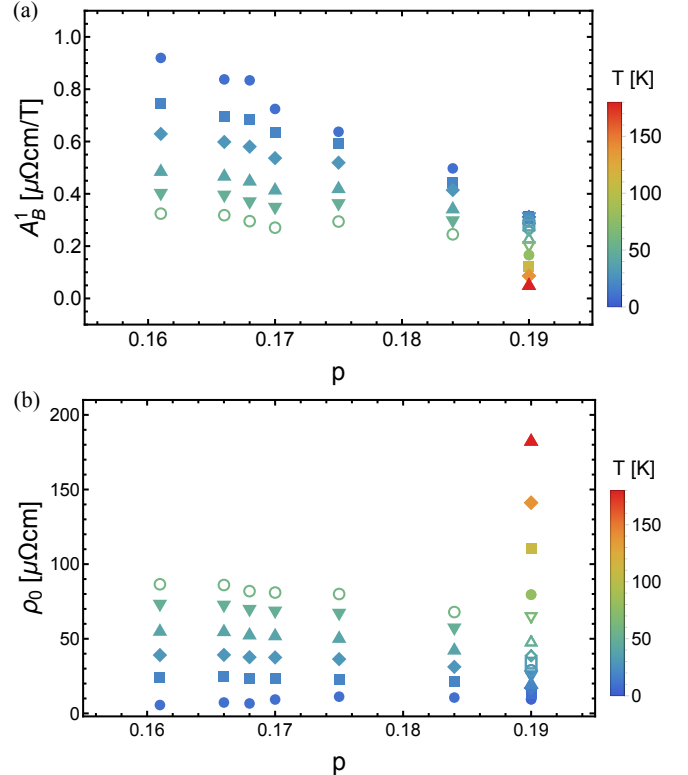


Figure 15. (a) Slope A_B^1 values and (b) zero-field residual resistivity ρ_0 obtained from the linear fit [Eq. (D12)] and plotted versus doping for the different temperature values. The color scheme corresponds to the temperature gradient shown in the bar legend. A_B^1 versus doping shows a monotonic, almost linear, decrease with doping for all temperature values as shown in Fig. 15 (a), which is consistent with the behavior of the linear-in-temperature coefficient A_T^1 [Fig. 13 (a)]. In Fig. 15 (b), we see that ρ_0 versus doping does not show any specific doping dependence.

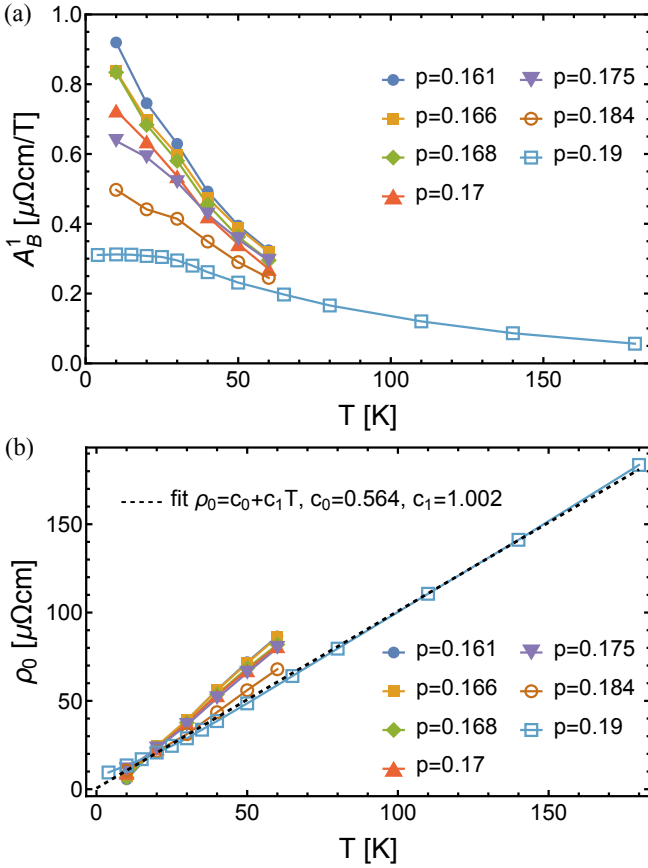


Figure 16. (a) Slope A_B^1 values and (b) zero-field residual resistivity ρ_0 obtained from the linear fit [Eq. (D12)] and plotted versus temperature for the different doping values. (a) A_B^1 versus temperature shows a monotonic decrease for all doping values. For $p = 0.19$, we observe a saturation plateau at low temperature, which is well described by our theoretical scaling function as shown in Fig. 9 and Fig. 2 (a) for different magnetic field values. For other doping values, magneto-resistivity data were only taken down to 10 K, which is unfortunately too high to see the appearance of the saturation plateau. (b) ρ_0 shows a linear temperature dependence for all doping. This implies that the zero-field resistivity contains a linear-in-temperature only dependence, introduced in the expression of the resistivity in Eq. (1) as $\rho_0(T) = c_0 + c_1 T$, which through the DC formula [Eq. (D2)] leads to an extra explicit temperature only dependence of the scattering rate expressed as $\hbar/\tau_0(T)$. This extra explicit temperature only dependence of the resistivity plays an important role when explaining the experimental data. Indeed as shown in Fig. 17 and Fig. 1 (a) in the main text, it allows to account for the slight change of the slope of the resistivity with respect to temperature.

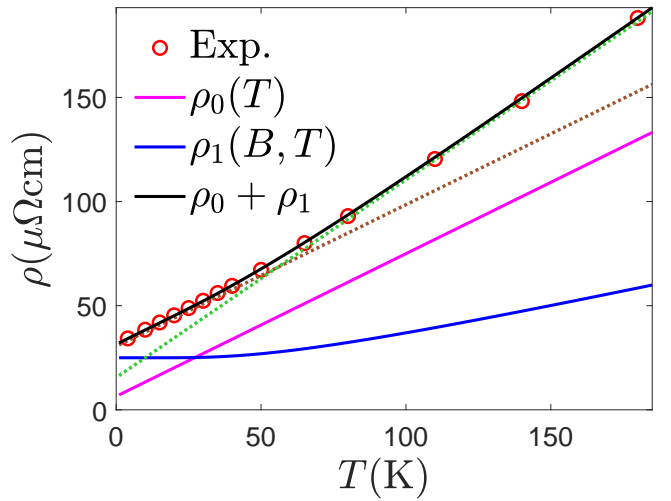


Figure 17. Different contributions of each of the terms in the theoretical expression for the resistivity in Eq. (1), compared to the experimental data at $p = 0.19$ and $B = 80\text{T}$ represented by the red circles. The pink line corresponds to the added temperature only dependence $\rho_0(T) = c_0 + c_1 T$, the blue line, which saturates at low temperatures, by the theoretical scaling function $\rho_1(B, T) = \frac{B}{\gamma} \coth \frac{\zeta \mu_B B}{2k_B T}$ and the total contribution by the black line. The parameters used in the theoretical prediction are the same as in Fig. 1 with $c_0 = 7.2\mu\Omega\text{cm}$, $c_1 = 0.654\mu\Omega\text{cmK}^{-1}$, $\gamma = 3.2(\mu\Omega\text{cm})^{-1}\text{T}$, $\zeta = 3.06$. The combination of the two contributions $\rho_0(T)$ and $\rho_1(B, T)$ results in a slight change of slope of the calculated resistivity around $T_{\text{kink}} \sim 60\text{ K}$, made more visually evident by the two dashed lines. This feature is also present in the experimental data, in excellent agreement with the theory.

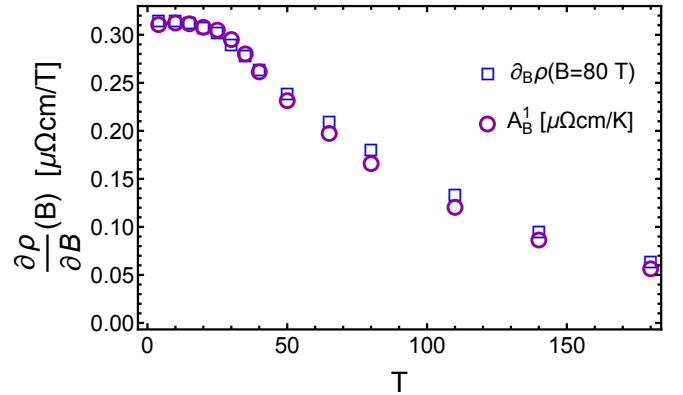


Figure 18. Slope of the resistivity data versus temperature for $p = 0.19$ using the values obtained by linear regression (purple circles) A_B^1 (purple circles) and the values obtained from the window slope analysis $\partial_B \rho(B = 80\text{T})$ method described in Appendix C at $B = 80\text{T}$ with a window width of $w = 22\text{T}$, corresponding to the saturation values of the slope in Fig. 6 (b) at $B = 80\text{T}$. The two methods are in good agreement.

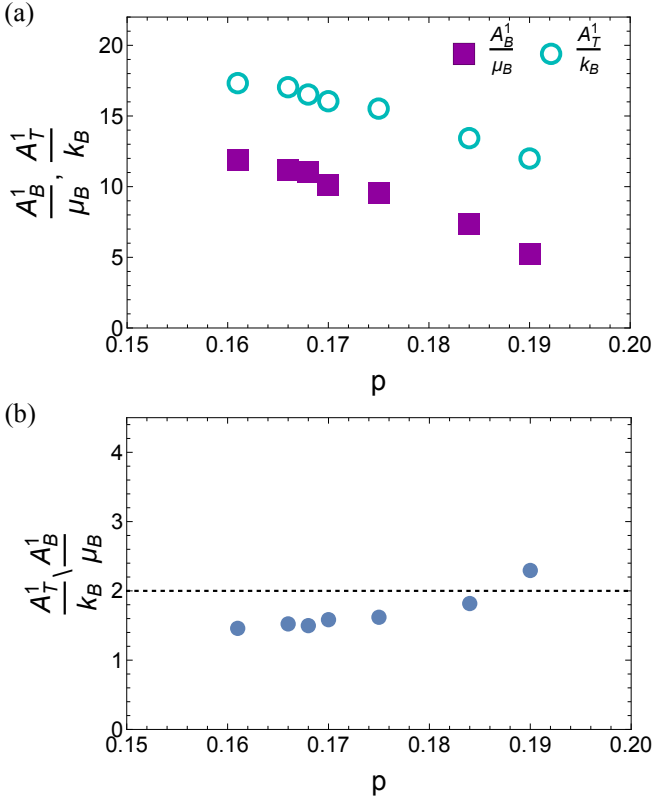


Figure 19. (a) Rescaled in-temperature A_T^1/k_B and in-field A_B^1/k_B slope coefficients obtained from linear regression of the experimental resistivity data plotted versus doping. Both the in-temperature A_T^1/k_B and in-field A_B^1/μ_B rescaled coefficients follow a similar trend with respect to doping, such that their ratio in (b) is almost doping independent. (b) ratio $A_T^1 \mu_B / (A_B^1 k_B)$ corresponding to the ratio of α_T/α_B [Eq. (D4)] versus doping in good agreement with our theoretical prediction yielding $\alpha_T/\alpha_B = 2$ (see Appendices B and C 2), denoted by the dashed black line. The slope values A_T^1 are further used through Eq. (D5)–Eq. (D10) to estimate the linear-in-temperature Planckian coefficients shown in Fig. 20

Appendix E: Scaling of AC resistivity

To extend our $B = T = 0$ result for $\Sigma''_\xi(\omega, B = T = 0)$, we now apply the conformal transformation assuming the system is in the quantum critical scaling regime.

We start from the equation below for the spectral representation of correlation function [41],

$$G_\psi(\tau) = - \int_{-\infty}^{\infty} \frac{e^{-\tau\varepsilon}}{1 + e^{-\beta\varepsilon}} A_\psi(\varepsilon) d\varepsilon, \quad (\text{E1})$$

where $0 \leq \tau \leq \beta$ and $A_\psi(\varepsilon) = (-1/\pi)G''_\psi(\omega + i0^+)$ denotes the spectral function for the ψ field. When a system has conformal invariance, any fermionic correlation function, such as the self-energy, in the imaginary-time domain can be

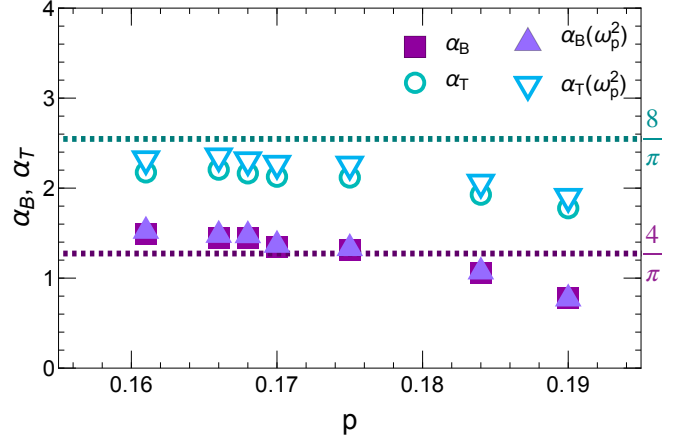


Figure 20. The linear-in-temperature (empty symbols) and linear-in-field (filled symbols) Planckian coefficients versus doping for LSCO obtained from magneto-resistivity data reproduced from [9]. Empty circles and filled squares correspond to the Planckian coefficients α_T and α_B obtained from the estimation of effective mass m^* from specific heat measurements as detailed above [Fig. 11]; while empty and filled triangles refer to Planckian coefficients obtained by measurements of the plasma frequency ω_p^2 denoted by $\alpha_T(\omega_p^2)$ and $\alpha_B(\omega_p^2)$. Horizontal purple and turquoise dashed lines correspond to theoretical prediction $\alpha_T = 8/\pi \simeq 2.54$ and $\alpha_B = 4/\pi \simeq 1.27$, respectively. For the experimental average value over doping for the Planckian coefficients we found $\langle \alpha_T^{\text{exp}} \rangle \simeq 2.07$, and $\langle \alpha_B^{\text{exp}} \rangle \simeq 1.27$ using effective mass estimations, and $\langle \alpha_T^{\text{exp}}(\omega_p^2) \rangle \simeq 2.17$ and $\langle \alpha_B^{\text{exp}}(\omega_p^2) \rangle \simeq 1.33$ from plasma frequency estimations, leading to a 5% discrepancy between the two methods.

expressed as [42]

$$\Sigma(\tau) \propto e^{\alpha(\tau/\beta-1/2)} \left[\frac{\pi/\beta}{\sin(\pi\tau/\beta)} \right]^{1+\nu}, \quad (\text{E2})$$

where α and ν are constants. Here, α is a measure of particle-hole asymmetry. Its spectral representation is given by

$$\begin{aligned} & e^{\alpha(\tau/\beta-1/2)} \left[\frac{\pi}{\sin(\pi\tau/\beta)} \right]^{1+\nu} \\ &= C_{\alpha,\nu} \int_{-\infty}^{\infty} dx \frac{e^{-x\tau/\beta}}{1 + e^{-x}} g_{\alpha,\nu}(x) \end{aligned} \quad (\text{E3})$$

with

$$\begin{aligned} g_{\alpha,\nu}(x) &= \left| \Gamma \left(\frac{1+\nu}{2} + i \frac{x+\alpha}{2\pi} \right) \right|^2 \\ &\times \frac{\cosh(x/2)}{\cosh(\alpha/2)\Gamma[(1+\nu)/2]^2}, \\ C_{\alpha,\nu} &= \frac{(2\pi)^\nu \cosh(\alpha/2)\Gamma[\frac{1+\nu}{2}]^2}{\pi\Gamma[1+\nu]}. \end{aligned} \quad (\text{E4})$$

Following Eqs. (E1)–(E4), we will generalize Σ_ξ that we obtain in the zero-temperature limit in the previous section to the finite-temperature one. We will further derive its ω/T scaling behavior once the finite-temperature generalization is

acquired. Applying Eq. (E1), we first evaluate the (imaginary) time dependence of Σ_ξ which shows a linear-in-frequency dependence in the frequency domain, $\Sigma_\xi \propto |\omega|$. It can be shown that Σ_ξ exhibits a τ^{-2} dependence:

$$\begin{aligned}\Sigma_\xi(\tau) &= \frac{1}{\pi} \int_{-\infty}^{\infty} \frac{|\varepsilon| e^{-\tau\varepsilon}}{1 + e^{-\beta\varepsilon}} d\varepsilon \\ &= \frac{1}{\pi} \left[\int_0^{\infty} |\varepsilon| e^{-\tau\varepsilon} + \int_{-\infty}^0 |\varepsilon| e^{(\beta-\tau)\varepsilon} \right] d\varepsilon \\ &= \frac{1}{\pi} \left[\frac{1}{\tau^2} \int_0^{\infty} |x| e^{-x} dx + \frac{1}{(\beta-\tau)^2} \int_{-\infty}^0 |x| e^x dx \right] \\ &= \frac{1}{\pi\tau^2}.\end{aligned}\quad (\text{E5})$$

It implies that this situation corresponds to the case of $\alpha = 0$ (particle-hole symmetric) and $\nu = 1$ (Planckian) as discussed in Refs. [41, 42]. The second term of the above equation vanishes when $T \rightarrow 0$. Once $\alpha = 0$ and $\nu = 1$ are decided, we can generalize Σ_ξ to the finite-temperature region by conformal transformation governed by Eqs. (E1)-(E4), leading to the following expression for $\Sigma_\xi(\omega, T)$,

$$\Sigma_\xi''(\omega, T) = \lambda_0 \beta^{-1} g_{0,1}(x) = \lambda_0 \frac{\omega}{2} \coth\left(\frac{\omega}{4T}\right) \quad (\text{E6})$$

with λ_0 being an unknown constant. λ_0 can be determined from its zero-temperature limit, where $\Sigma_\xi''(\omega, T = 0) = -(2/\pi)|\omega|$. We thus find $\lambda_0 = -4/\pi$, leading to

$$\Sigma_\xi''(\omega, T) = \lambda_0 \beta^{-1} g_{0,1}(x) = -\frac{4}{\pi} \left[\frac{\omega}{2} \coth\left(\frac{\omega}{4T}\right) \right]. \quad (\text{E7})$$

Using the relation of $\Sigma_c = (1/2)\Sigma_\xi$, the scattering rate for the conduction c electron can be obtained by $\hbar/\tau_c = -2\Sigma_c''(\omega)$ (here we restore \hbar and k_B), $\frac{\hbar}{\tau_c} = \frac{4}{\pi} \left[\frac{\hbar\omega}{2} \coth\left(\frac{\hbar\omega}{4k_B T}\right) \right]$. It shows the following frequency-to-temperature scaling behavior

$$\frac{\hbar/\tau_c}{k_B T} = \frac{4}{\pi} \left[\frac{x}{2} \coth\left(\frac{x}{4}\right) \right], \quad (\text{E8})$$

where $x \equiv \hbar\omega/k_B T$.

Note that the ω/T -scaling function in scattering rate at finite frequency and temperature is not uniquely determined by the zero-temperature conduction electron self-energy $\Sigma_\xi''(\omega, T = 0)$ via conformal mapping by Eqs. (E1)-(E4). We find that in general the scaling function $\frac{\hbar/\tau}{k_B T} = \frac{2x}{\pi} \coth\frac{x}{2p}$ for $p \geq 1$ reduces to the same zero-temperature scattering rate $1/\tau(\omega, T = 0) = -2\Sigma_\xi''(\omega, T = 0) = \frac{2}{\pi}\omega$ in the limit of $\frac{k_B T}{\hbar\omega} \rightarrow 0$ (see also Fig. S1 in Ref. [21]).

[1] A. Legros, S. Benhabib, W. Tabis, F. Laliberté, M. Dion, M. Lizaire, B. Vignolle, D. Vignolles, H. Raffy, Z. Z. Li, P. Auban-Senzier, N. Doiron-Leyraud, P. Fournier, D. Colson, L. Taillefer, and C. Proust, *Nat. Phys.* **15**, 142 (2019).

[2] N. Doiron-Leyraud, S. René de Cotret, A. Sedeki, C. Bourbonnais, L. Taillefer, P. Auban-Senzier, D. Jérôme, and K. Bechgaard, *Eur. Phys. J. B* **78**, 23 (2010).

[3] B. Michon, C. Berthod, C. W. Rischau, A. Ataei, L. Chen, S. Komiya, S. Ono, L. Taillefer, D. van der Marel, and A. Georges, *Nature Communications* **14**, 3033 (2023).

[4] C. Proust and L. Taillefer, *Annual Review of Condensed Matter Physics* **10**, 409 (2019).

[5] B. Michon, C. Girod, S. Badoux, J. Kačmarčík, Q. Ma, M. Dragomir, H. A. Dabkowska, B. D. Gaulin, J. S. Zhou, S. Pyon, T. Takayama, H. Takagi, S. Verret, N. Doiron-Leyraud, C. Marcenat, L. Taillefer, and T. Klein, *Nature* **567**, 218 (2019).

[6] S. Badoux, W. Tabis, F. Laliberté, G. Grissonnac, B. Vignolle, D. Vignolles, J. Béard, D. A. Bonn, W. N. Hardy, R. Liang, N. Doiron-Leyraud, L. Taillefer, and C. Proust, *Nature* **531**, 210 (2016).

[7] C. Collignon, S. Badoux, S. A. Afshar, B. Michon, F. Laliberté, O. Cyr-Choinière, J. S. Zhou, S. Licciardello, S. Wiedmann, N. Doiron-Leyraud, and L. Taillefer, *Physical Review B* **95**, 224517 (2017).

[8] A. Shekhter, B. J. Ramshaw, M. K. Chan, and N. Harrison, *Universal planckian relaxation in the strange metal state of the cuprates* (2025), arXiv:2406.12133 [cond-mat.str-el].

[9] P. Giraldo-Gallo, J. A. Galvis, Z. Stegen, K. A. Modic, F. F. Balakirev, J. B. Betts, X. Lian, C. Moir, S. C. Riggs, J. Wu, A. T. Bollinger, X. He, I. Božović, B. J. Ramshaw, R. D. McDonald, G. S. Boebinger, and A. Shekhter, *Science* **361**, 479 (2018).

[10] J. Ayres, M. Berben, M. Čulo, Y.-T. Hsu, E. van Heumen, Y. Huang, J. Zaanen, T. Kondo, T. Takeuchi, J. R. Cooper, C. Putzke, S. Friedemann, A. Carrington, and N. E. Hussey, *Nature* **595**, 661 (2021).

[11] J. Ayres, M. Berben, C. Duffy, R. D. H. Hinlopen, Y.-T. Hsu, A. Cuoghi, M. Leroux, I. Gilmutdinov, M. Massoudzadegan, D. Vignolles, Y. Huang, T. Kondo, T. Takeuchi, S. Friedemann, A. Carrington, C. Proust, and N. E. Hussey, *Nature Communications* **15**, 8406 (2024).

[12] A. A. Abrikosov, *Fundamentals of the Theory of Metals* (North-Holland, 1988).

[13] A. B. Pippard, *Magnetoresistance in Metals* (Cambridge Univ. Press, 1989).

[14] A. Ataei, A. Gourgout, G. Grissonnac, L. Chen, J. Baglo, M.-E. Boulanger, F. Laliberté, S. Badoux, N. Doiron-Leyraud, V. Oliviero, S. Benhabib, D. Vignolle, J.-S. Zhou, S. Ono, H. Takagi, C. Proust, and L. Taillefer, *Nat. Phys.* **18**, 1420–1424 (2022).

[15] A. A. Patel, J. McGreevy, D. P. Arovas, and S. Sachdev, *Phys. Rev. X* **8**, 021049 (2018).

[16] J. Kim, E. Altman, and S. Chatterjee, *Proceedings of the National Academy of Sciences* **121**, e2405720121 (2024).

[17] H. Alloul, *Frontiers in Physics* **Volume 12** - 2024, 10.3389/fphy.2024.1406242 (2024).

[18] Y.-Y. Chang, K. V. Nguyen, K. Remund, and C.-H. Chung, *Reports on Progress in Physics* **88**, 048001 (2025).

[19] H. Takagi, B. Batlogg, H. L. Kao, J. Kwo, R. J. Cava, J. J. Krajewski, and W. F. Peck, *Phys. Rev. Lett.* **69**, 2975 (1992).

[20] S. D. Chen, M. Hashimoto, Y. He, D. Song, K. J. Xu, J. F. He, T. P. Devereaux, H. Eisaki, D. H. Lu, J. Zaanen, and Z. X. Shen, *Science* **366**, 1099 (2019).

[21] Y.-Y. Chang, K. V. Nguyen, K. Remund, and C.-H. Chung, *Theory of universal planckian metal in t - j model: application for high- t_c cuprate superconductors* (2025), arXiv:2506.15552 [cond-mat.str-el].

[22] T. R. Chien, Z. Z. Wang, and N. P. Ong, *Phys. Rev. Lett.* **67**, 2088 (1991).

[23] T. R. Chien, D. A. Brawner, Z. Z. Wang, and N. P. Ong, *Phys. Rev. B* **43**, 6242 (1991).

[24] Y. Ando, Y. Kurita, S. Komiya, S. Ono, and K. Segawa, *Phys. Rev. Lett.* **92**, 197001 (2004).

[25] G. Grissonnanche, Y. Fang, A. Legros, S. Verret, F. Laliberté, C. Collignon, J. Zhou, D. Graf, P. A. Goddard, L. Taillefer, and B. J. Ramshaw, *Nature* **595**, 667 (2021).

[26] C. M. Varma, P. B. Littlewood, S. Schmitt-Rink, E. Abrahams, and A. E. Ruckenstein, *Physical Review Letters* **63**, 1996 (1989).

[27] N. W. Ashcroft and N. D. Mermin, *Solid State Physics* (Holt-Saunders, 1976).

[28] W. J. Padilla, Y. S. Lee, M. Dumm, G. Blumberg, S. Ono, K. Segawa, S. Komiya, Y. Ando, and D. N. Basov, *Phys. Rev. B* **72**, 060511 (2005).

[29] A. Legros, K. W. Post, P. Chauhan, D. G. Rickel, X. He, X. Xu, X. Shi, I. Božović, S. A. Crooker, and N. P. Armitage, *Phys. Rev. B* **106**, 195110 (2022).

[30] Y. Zhong, Z. Chen, S.-D. Chen, K.-J. Xu, M. Hashimoto, Y. He, S. ichi Uchida, D. Lu, S.-K. Mo, and Z.-X. Shen, *Proceedings of the National Academy of Sciences* **119**, e2204630119 (2022).

[31] M. Berben, J. Ayres, C. Duffy, R. D. H. Hinlopen, Y. T. Hsu, M. Leroux, I. Gilmutdinov, M. Massoudzadegan, D. Vignolles, Y. Huang, T. Kondo, T. Takeuchi, J. R. Cooper, S. Friedemann, A. Carrington, C. Proust, and N. E. Hussey, *Compartmentalizing the cuprate strange metal* (2022), arXiv:2203.04867 [cond-mat.supr-con].

[32] Y. Ando, G. S. Boebinger, A. Passner, T. Kimura, and K. Kishio, *Phys. Rev. Lett.* **75**, 4662 (1995).

[33] Y. Ando, G. S. Boebinger, A. Passner, L. F. Schneemeyer, T. Kimura, M. Okuya, S. Watauchi, J. Shimoyama, K. Kishio, K. Tamasaku, N. Ichikawa, and S. Uchida, *Phys. Rev. B* **60**, 12475 (1999).

[34] S. Caprara, M. Grilli, J. Lorenzana, and B. Leridon, *SciPost Phys.* **8**, 003 (2020).

[35] J. Brunkert and M. Punk, *Phys. Rev. Res.* **2**, 43019 (2020).

[36] M. Punk, A. Allais, and S. Sachdev, *Proceedings of the National Academy of Sciences* **112**, 9552 (2015).

[37] T. Senthil, S. Sachdev, and M. Vojta, *Physical Review Letters* **90**, 216403 (2003).

[38] S. S. Lee, *Physical Review B - Condensed Matter and Materials Physics* **78**, 085129 (2008).

[39] A. Shekhter, K. A. Modic, L. E. Winter, Y. Lai, M. K. Chan, F. F. Balakirev, J. B. Betts, S. Komiya, S. Ono, G. S. Boebinger, B. J. Ramshaw, and R. D. McDonald, *Energy-scale competition in the hall resistivity of a strange metal* (2022), arXiv:2207.10244 [cond-mat.str-el].

[40] J. Loram, J. Luo, J. Cooper, W. Liang, and J. Tallon, *Journal of Physics and Chemistry of Solids* **62**, 59 (2001).

[41] O. Parcollet, A. Georges, G. Kotliar, and A. Sengupta, *Phys. Rev. B* **58**, 3794 (1998).

[42] A. Georges and J. Mravlje, *Phys. Rev. Research* **3**, 43132 (2021).